

AD-A142 737

MIE SCATTERING AS A TECHNIQUE FOR THE SIZING OF AIR  
BUBBLES(U) MISSISSIPPI UNIV UNIVERSITY PHYSICAL  
ACOUSTICS RESEARCH LAB G M HANSEN ET AL. 01 JUN 84

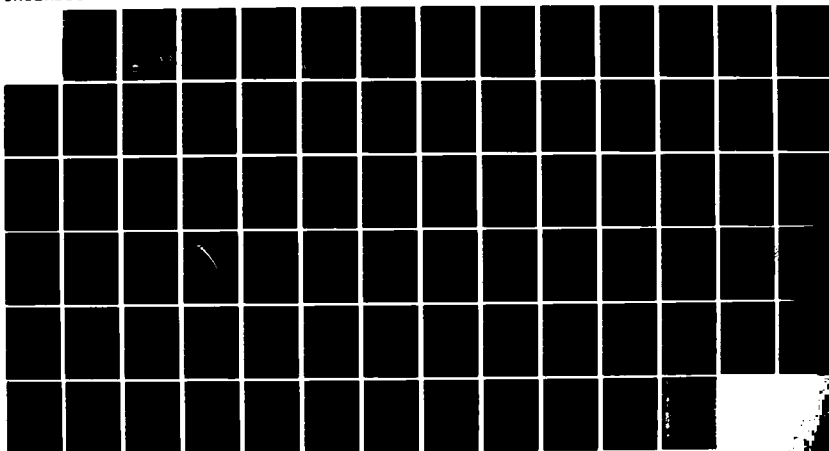
1/1

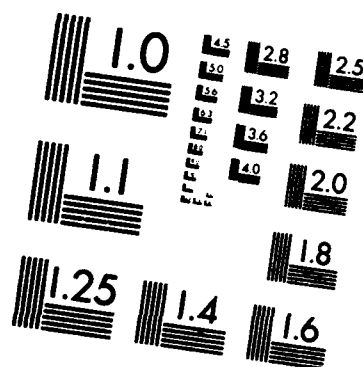
UNCLASSIFIED

TR-1-84 N00014-84-C-0193

F/G 20/6

NL





MICROCOPY RESOLUTION TEST CHART  
NATIONAL BUREAU OF STANDARDS-1963-A

AD-A142 737

MIE SCATTERING AS A  
TECHNIQUE FOR THE  
SIZING OF AIR BUBBLES

DTIC FILE COPY

DTIC  
ELECTE  
JUL 06 1984  
S D E



THE UNIVERSITY OF MISSISSIPPI  
PHYSICAL ACOUSTICS RESEARCH GROUP  
DEPARTMENT OF PHYSICS AND ASTRONOMY

This document has been approved  
for public release and sales in  
distribution is unlimited.

84 07 05 054

Approved for Public Release: Distribution Unlimited

Technical Report for  
Office of Naval Research  
Contract N00014-84-C-0193

MIE SCATTERING AS A  
TECHNIQUE FOR THE  
SIZING OF AIR BUBBLES

by

G. M. Hansen\* and L. A. Crum  
Physical Acoustics Research Laboratory  
Department of Physics and Astronomy  
The University of Mississippi  
University, MS 38677

June 1, 1983

DTIC  
ELECTE  
JUL 06 1984  
S D  
E

\*Ph. D. Dissertation directed by L. A. Crum.

Reproduction in whole or in part is permitted for any  
purpose by the U. S. Government

This document has been approved  
for public release and sale; its  
distribution is unlimited.

Unclassified

SECURITY CLASSIFICATION OF THIS PAGE (When Data Entered)

REPORT DOCUMENTATION PAGE		READ INSTRUCTIONS BEFORE COMPLETING FORM
1. REPORT NUMBER 1-84	2. GOVT ACCESSION NO. AD-A172737	3. RECIPIENT'S CATALOG NUMBER
4. TITLE (and Subtitle) Mie Scattering as a Technique for the Sizing of Air Bubbles		5. TYPE OF REPORT & PERIOD COVERED Technical
		6. PERFORMING ORG. REPORT NUMBER
7. AUTHOR(s) G. M. Hansen and L. A. Crum		8. CONTRACT OR GRANT NUMBER(s) N00014-84-C-0193
9. PERFORMING ORGANIZATION NAME AND ADDRESS Physical Acoustics Research Laboratory Department of Physics University of Mississippi, University, MS 38677		10. PROGRAM ELEMENT, PROJECT, TASK AREA & WORK UNIT NUMBERS
11. CONTROLLING OFFICE NAME AND ADDRESS Office of Naval Research, Physics Div. Code 412, Arlington, VA 22217		12. REPORT DATE 6-1-84
		13. NUMBER OF PAGES 69
14. MONITORING AGENCY NAME & ADDRESS (if different from Controlling Office)		15. SECURITY CLASS. (of this report) Unclassified
		15a. DECLASSIFICATION/DOWNGRADING SCHEDULE
16. DISTRIBUTION STATEMENT (of this Report)  Approved for public release; distribution unlimited		
17. DISTRIBUTION STATEMENT (of the abstract entered in Block 20, if different from Report)		
18. SUPPLEMENTARY NOTES		
19. KEY WORDS (Continue on reverse side if necessary and identify by block number)  Mie scattering Bubbles Nonlinear Oscillations  Acoustic Cavitation		
20. ABSTRACT (Continue on reverse side if necessary and identify by block number) → A technique has been developed which allows the radius of a bubble in a fluid to be accurately measured without disturbing the bubble. Results are presented which show that radius measurements of single air-bubbles in water can be achieved by shining a He-Ne laser on the bubble and measuring the light scattered at 80 degrees. Light intensity measurements at a scattering angle of 55 degrees were used to calibrate a photodiode detection system and to demonstrate the correlation of data with Mie scattering theory. The		

DD FORM 1473

1 JAN 73

EDITION OF 1 NOV 65 IS OBSOLETE

S/N 0102-LF-014-6601

Unclassified

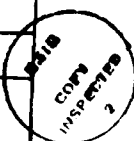
SECURITY CLASSIFICATION OF THIS PAGE (When Data Entered)

Unclassified

SECURITY CLASSIFICATION OF THIS PAGE (When Data Entered)

photodiode was then moved to 80 degrees for actual radius measurements. This technique was accurate to within 3% for bubbles with radii less than 80 microns.

Accession For	
NTIS GRA&I	<input checked="checked" type="checkbox"/>
DTIC TAB	<input type="checkbox"/>
Unannounced	<input type="checkbox"/>
Justification	
By	
Distribution/	
Availability Codes	
Dist	Avail and/or Special
A-1	



S/N 0102- LF-014-6601

Classified

SECURITY CLASSIFICATION OF THIS PAGE (When Data Entered)

#### ACKNOWLEDGMENTS

I wish to express my gratitude to my research advisor, Dr. Lawrence Crum, for things too numerous to mention.

I would like to thank the members of my committee; Dr. Henry Bass, Dr. Allen Glisson, Dr. Thomas Marshall, and Dr. John Tarvin; for their time and their helpful editorial comments.

I would also like to thank Dr. Philip Marston for sending reprints and preprints of his work.

Thanks to the research members of my lab group; Anthony Atchley, Brian Fowlkes and Ron Roy for the conversations, general enthusiasm, and sometimes lunacy.

Thanks to the Office of Naval Research and the National Science Foundation for the funding which made this project possible.

A special thanks to Miss Rita Gariboldi for everything.

## TABLE OF CONTENTS

	Page
LIST OF FIGURES .....	v
INTRODUCTION .....	1
 Section	
I. THEORY .....	5
A. Rise-velocity method .....	5
B. Mie scattering .....	8
C. Far field solution .....	19
D. Calculation methods .....	21
E. Computational results .....	27
II. EXPERIMENTAL .....	40
A. Apparatus .....	40
B. Procedure .....	46
C. Results .....	51
III. DISCUSSION .....	55
REFERENCES .....	61
APPENDIX A. COMPUTER PROGRAM USED FOR MIE-SCATTERING CALCULATIONS ..	64
BIOGRAPHICAL SKETCH OF THE AUTHOR .....	69



## LIST OF FIGURES

Figure	Page
1. Bubble radius calculated from rise-velocity and three different drag laws .....	7
2a. Variation of gain with angle, radius = 50 $\mu\text{m}$ .....	28
2b. Variation of gain with angle, radius = 50 $\mu\text{m}$ .....	29
2c. Variation of gain with angle, radius = 50 $\mu\text{m}$ .....	30
2d. Variation of gain with angle, radius = 50 $\mu\text{m}$ .....	31
3. Variation of gain with angle for radius = 50 $\mu\text{m}$ and 51 $\mu\text{m}$ .....	32
4. Variation of gain with radius for scattering angles 20 and 30 degrees .....	33
5. Relative intensity as a function of radius at a scattering angle of 55 degrees .....	35
6. Relative intensity as a function of radius at a scattering angle of 80 degrees .....	36
7. Results of numerical integration of intensity from 54 to 56 degrees as a function of radius .....	37
8. Results of numerical integration of intensity from 79 to 81 degrees as a function of radius .....	39
9. Block diagram of experimental setup .....	41
10. Laser Beam profile taken with 1.6 mm aperture .....	42
11. Scale drawing (1:1) of the acoustic levitation cell .....	43
12. Photodiode circuit .....	44
13. Experimental points and theoretical curve of .04 mm single slit diffraction pattern .....	47

## Figure

## Page

14. Light intensity from bubbles as a function of radius obtained  
by rise-velocity method, scattering angle = 55 degrees ..... 52
15. Intensity and radius with data shifted to match theory at  
56.9  $\mu\text{m}$  ..... 53
16. Intensity and radius at scattering angle = 80 degrees, same  
shift as in Fig. 15 ..... 54

..

## INTRODUCTION

The need for a bubble radius measurement technique that is accurate and does not disturb the bubble has been brought about by theoretical and experimental studies of bubble oscillations.<sup>1-8</sup> For instance, theoretical work on nonlinear oscillations of gas bubbles in liquids by Prosperetti<sup>1</sup> predicts that individual bubbles subjected to an acoustic field will have harmonic resonances in their pulsation amplitude. These resonances occur when an oscillating bubble's radius is equal to the resonance radius for frequencies that are harmonics of the driving frequency. Some experimental work has been presented by Crum and Prosperetti<sup>8</sup> to verify these predictions, but the evidence is inconclusive. A rise-velocity technique was used to measure bubble radii which, they state, could be in error by as much as 10%.

Another example is the prediction of the rectified diffusion threshold for various combinations of the bubble radius, oscillation frequency, and acoustic pressure amplitude.<sup>6</sup> Rectified diffusion is the process whereby a bubble will grow (under proper conditions) when subjected to an acoustic pressure. While there are some indirect indications of the validity of these predictions,<sup>9</sup> direct measurements on single bubbles have employed the rise-velocity method which is subject to error.

The rise-velocity method is the calculation of a bubble's radius from a measurement of its terminal rise-velocity. There are, however, certain

inherent difficulties with this method. First, to calculate the radius the drag force acting on the bubble must be known. The drag force is related to a drag coefficient and there are dozens of different empirical drag "laws"<sup>10</sup> that are based on rigid spheres in which compressibility and wall effects are ignored. As a result large radius differences can be found, for the same terminal velocity, when using different drag laws. Second, determining the terminal velocity can be difficult. For example, in the method used by Crum,<sup>4</sup> the bubble is started from rest and its time to rise a certain distance is recorded. There is a reaction time involved in stopping the timer which can be a source of error as great as 5%. Also, the bubble's initial acceleration is assumed to be negligible. Third, bubbles that are large enough to rise continually dissolve. For example, a 20  $\mu\text{m}$  bubble is observed to dissolve in about 10 seconds in water that is not supersaturated with gas. Thus the radius changes during the measurement. Accounting for this change is difficult, since the rate at which bubbles dissolve is dependent on many parameters.<sup>11</sup> This dissolution is particularly a problem when the behavior of the bubble in a sound field is being investigated. To let the bubble rise "freely" with only buoyancy, drag, and weight acting on it, the sound field must be turned off for the period of rise. During this zero acoustic-pressure time the bubble will dissolve slightly.

A different technique for measuring bubble radii is presented in an experiment conducted by Marston.<sup>12</sup> In it a photograph is taken of the light scattered from an air bubble in water. This photo is scanned with a microdensitometer to obtain the intensity variation with angle. The

photo pattern is then compared to the pattern predicted by a physical optics approximation to the Mie scattering theory. This same technique has recently been refined and used to correlate photographic patterns with predicted patterns for measured bubble sizes from 25 to 1000 microns.<sup>13</sup>

It was the difficulties with the rise-velocity method coupled with Marston's work on light scattering from air bubbles that led to the present investigation.

The solution for scattering of electromagnetic waves by a sphere is generally referred to as the "Mie theory", named after Gustav Mie, although the derivation had been worked out by Debye<sup>14</sup> at about the same time. Mie's original paper<sup>15</sup> addresses the then long-standing problem of accounting for the brilliant color exhibited by colloiddally dispersed metal particles.

The Mie scattering theory is used in various ways in diversified fields such as atmospheric optics,<sup>16-19</sup> astrophysics,<sup>20,21</sup> and physical chemistry.<sup>22,23</sup> Much of this work is concerned with the scattering of electromagnetic radiation by distributions of particles of various sizes. Also, most of the work is concentrated on particles whose index of refraction is greater than that of their surroundings. Only recently has any extensive work been carried out on the case of air bubbles in water.<sup>12,13,24</sup> Studies on the determination of the average size of the particles in the distributions are based primarily on the measure of the angular intensity variations. There is, however, at least one study in

which Holve and Self<sup>25</sup> measure particle size distributions using pulse height analysis on near-forward scattered light. Two excellent books have been written on the subject of Mie scattering and serve as excellent reviews of the work previously conducted.<sup>26,27</sup>

This dissertation deals with the development of a method to measure the radius of a single air bubble in water through the measurement of the light intensity scattered at a single angle.

Section I contains the theory behind the measurements to be made. First, the equations which allow the rise-velocity to be used for radius measurements are derived. Next, the theory for electromagnetic radiation scattered by a spherical object is briefly explained. The scattering functions are derived and the far-field solution which is needed to describe the experimental situation is given. The calculation method is described, and other necessary equations are presented. Finally, the computational results are presented.

Section II presents the experimental portion of the study and consists of an explanation of the apparatus and the procedures used, along with the experimental results.

Section III discusses the results of the experiment. Some suggestions for further studies and possible improvements in the experimental design are also addressed.

## I. THEORY

### A. Rise-velocity method

For a bubble rising in water at terminal velocity  $U$ , the forces of buoyancy, weight and drag are balanced. The drag force is<sup>28</sup>

$$F_D = \frac{1}{2} \rho U^2 \pi a^2 C_D, \quad (1)$$

where  $\rho$  is the density of the water,  $a$  is the radius of the bubble, and  $C_D$  is the drag coefficient. The equation of balanced forces is

$$\frac{4}{3} \pi a^3 \sigma g + \frac{1}{2} \rho U^2 \pi a^2 C_D = \frac{4}{3} \pi a^3 \rho g, \quad (2)$$

where  $\sigma$  is the density of the air in the bubble and  $g$  is the acceleration due to gravity. From this equation we find that

$$a = \frac{3}{8} \frac{U^2}{g} C_D, \quad (3)$$

since  $\rho/(\rho - \sigma) \approx 1$ .

The drag coefficient is expressed as a function of the Reynolds number  $Re = 2aU/\nu$ , where  $\nu$  is the kinematic coefficient of viscosity of the fluid and is defined as  $\mu/\rho$ , where  $\mu$  is the dynamic viscosity and  $\rho$  is the density. The drag coefficient has been calculated by Stokes,<sup>28</sup> for rigid spheres, to be  $24/Re$ , which is valid for low Reynolds numbers. Many other drag laws have been determined empirically.<sup>10</sup> The law used for the rise-velocity calculations in this

study was determined by Schiller and Nauman<sup>10</sup> and was chosen because it matched the "standard drag curve" fairly well for the region of interest. The form of this law is

$$C_D = \frac{24}{Re} (1 + 0.15Re^{0.687}) . \quad (4)$$

For comparison purposes the law determined by Langmuir and Blodgett<sup>10</sup> which was used by Crum and Eller<sup>29</sup> is given by

$$C_D = \frac{24}{Re} (1 + 0.197Re^{0.63} + 2.6 \times 10^{-4}Re^{1.38}) . \quad (5)$$

With each of these drag laws an iterative method must be used to obtain the radius. The results of such calculations for the three different drag laws given above and a large range of bubble sizes is shown in Fig. 1. The temperature used for these data was 25°C. Note the large differences in radius for large rise velocities (about 7  $\mu\text{m}$  at 0.7 cm/s rise velocity). This graph shows one of the inherent problems in using this method to determine the bubble radius.



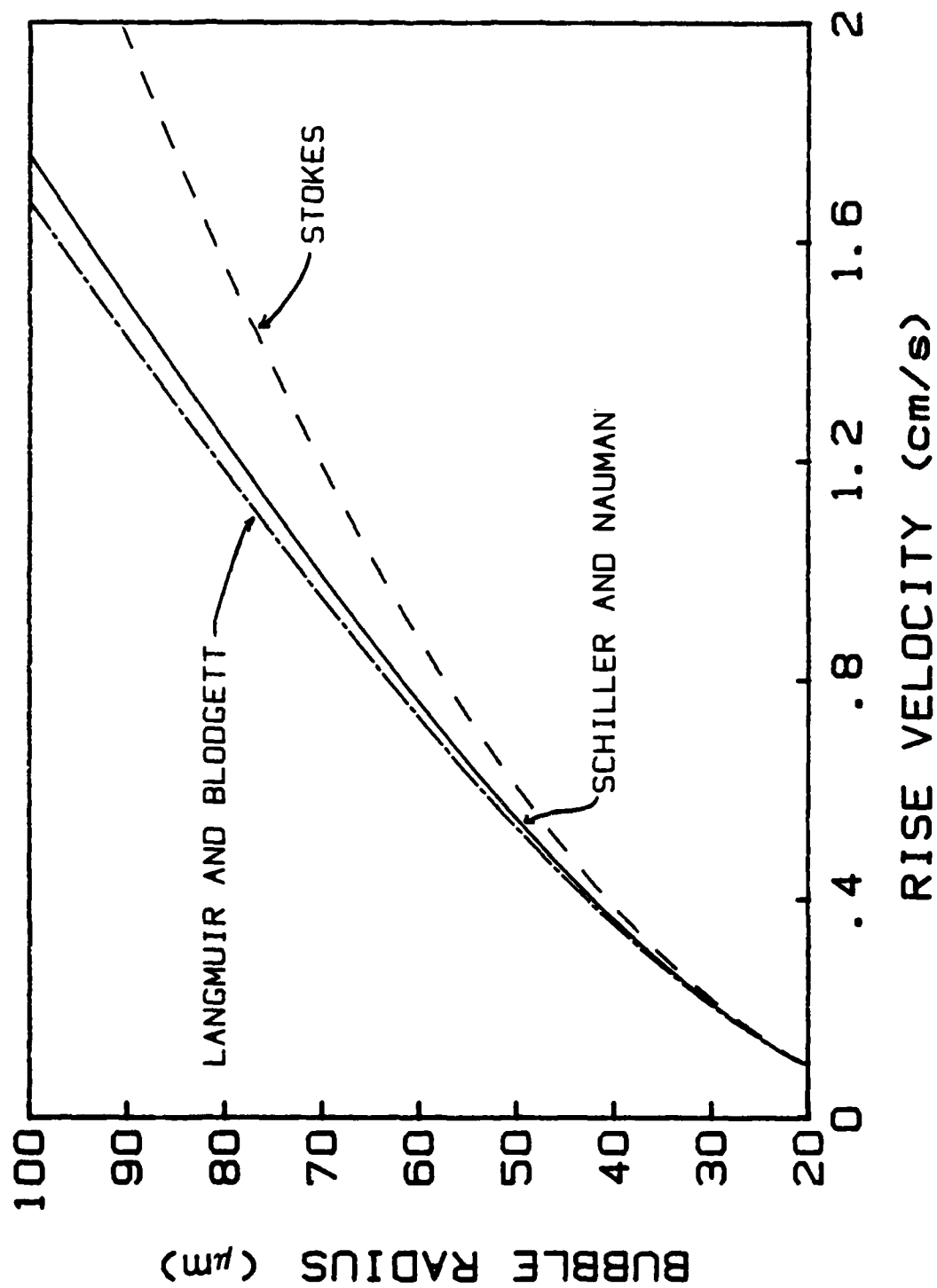


FIG. 1. Bubble radius calculated from rise-velocity and three different drag laws.

## B. Mie scattering

Extensive analysis of the scattering of light by a spherical object can be found in Born and Wolfe<sup>30</sup> and Stratton<sup>31</sup> as well as in the original works of Debye<sup>14</sup> and Mie.<sup>15</sup> The following contains the essence of these calculations. The potential approach will be used rather than dealing directly with the vector wave equation.

The system under consideration is a non-conducting sphere (medium 1), radius  $a$ , immersed in a homogeneous, isotropic medium (medium 2) within which there are no conduction currents nor free charges, with a plane, linearly polarized, monochromatic wave impinging upon it. The field equations under these conditions are

$$\bar{\nabla} \times \bar{E} + \frac{\partial \bar{B}}{\partial t} = 0 , \quad (6a)$$

$$\bar{\nabla} \times \bar{H} - \frac{\partial \bar{D}}{\partial t} = 0 , \quad (6b)$$

$$\bar{\nabla} \cdot \bar{D} = 0 , \quad (6c)$$

$$\text{and} \quad \bar{\nabla} \cdot \bar{B} = 0 , \quad (6d)$$

with  $\bar{D} = \epsilon \bar{E}$ , and  $\bar{B} = \mu \bar{H}$ .

These equations can be reduced to the determination of a vector potential,  $\bar{A}$ , and a scalar potential,  $\phi$ , from which the fields are found through the use of the equations

$$\bar{B} = \bar{\nabla} \times \bar{A} , \quad (7a)$$

$$\text{and} \quad \bar{E} = -\bar{\nabla}\phi - \frac{\partial \bar{A}}{\partial t} . \quad (7b)$$

It is also possible to define an electromagnetic field in terms of a single vector function. Assume that the vector potential  $\bar{A}$  is proportional to the time derivative of a vector  $\bar{\Pi}_1$  such that

$$\bar{A} = \mu\epsilon \frac{\partial \bar{\Pi}_1}{\partial t}. \quad (8)$$

Consequently

$$\bar{B} = \mu\epsilon \bar{\nabla} \times \frac{\partial \bar{\Pi}_1}{\partial t}, \quad (9a)$$

and

$$\bar{E} = -\bar{\nabla}\phi - \mu\epsilon \frac{\partial^2 \bar{\Pi}_1}{\partial t^2}. \quad (9b)$$

Substituting these expressions for  $\bar{E}$  and  $\bar{B}$  into Eq. (6b) results in

$$\frac{\partial}{\partial t} (\bar{\nabla} \times \bar{\nabla} \times \bar{\Pi}_1 + \bar{\nabla}\phi + \mu\epsilon \frac{\partial^2 \bar{\Pi}_1}{\partial t^2}) = 0. \quad (10)$$

The choice of the scalar potential,  $\phi$ , is arbitrary so long as it satisfies

$$\nabla^2 \phi - \mu\epsilon \frac{\partial^2 \phi}{\partial t^2} = 0. \quad (11)$$

Therefore,

$$\phi = -\bar{\nabla} \cdot \bar{\Pi}_1 \quad (12)$$

is chosen. Integrating Eq. (10), with respect to time, gives

$$\bar{\nabla} \times \bar{\nabla} \times \bar{\Pi}_1 - \bar{\nabla}(\bar{\nabla} \cdot \bar{\Pi}_1) + \mu\epsilon \frac{\partial^2 \bar{\Pi}_1}{\partial t^2} = \text{constant}. \quad (13)$$

Since the particular value of the constant does not affect the

determination of the field, the constant is chosen to be zero. Then every solution to Eq. (13) determines an electromagnetic field through the equations

$$\bar{\mathbf{B}} = \mu\epsilon \bar{\nabla} \times \frac{\partial \bar{\Pi}_1}{\partial t}, \quad (14a)$$

and 
$$\bar{\mathbf{E}} = \bar{\nabla}(\bar{\nabla} \cdot \bar{\Pi}_1) - \mu\epsilon \frac{\partial^2 \bar{\Pi}_1}{\partial t^2}. \quad (14b)$$

Using a well-known vector identity Eq. (13) may be rewritten as

$$\nabla^2 \bar{\Pi}_1 - \mu\epsilon \frac{\partial^2 \bar{\Pi}_1}{\partial t^2} = 0. \quad (15)$$

An alternate solution,  $\bar{\Pi}_2$ , may also be chosen by writing

$$\bar{\mathbf{D}} = -\mu\epsilon \bar{\nabla} \times \frac{\partial \bar{\Pi}_2}{\partial t}, \quad (16a)$$

and 
$$\bar{\mathbf{H}} = \bar{\nabla}(\bar{\nabla} \cdot \bar{\Pi}_2) - \mu\epsilon \frac{\partial^2 \bar{\Pi}_2}{\partial t^2}, \quad (16b)$$

and by choosing the potentials to be

$$\bar{A}_2 = \mu\epsilon \frac{\partial \bar{\Pi}_2}{\partial t}, \quad (17a)$$

and 
$$\phi_2 = -\bar{\nabla} \cdot \bar{\Pi}_2. \quad (17b)$$

Thus the electromagnetic field within our region can be resolved into two partial fields, one derived from  $\bar{\Pi}_1$ , the other from  $\bar{\Pi}_2$ . The source of the electromagnetic field derived from the vector  $\bar{\Pi}_1$  is a distribution of electric polarization. This can be seen by writing  $\bar{\mathbf{D}} = \epsilon_0 \bar{\mathbf{E}} + \bar{\mathbf{P}}$ , where  $\bar{\mathbf{D}}$  is the displacement current and  $\bar{\mathbf{P}}$  the polarization,

and replacing Eqs. (6b) and (6c) with

$$\bar{\nabla} \times \bar{H} - \epsilon_0 \frac{\partial \bar{E}}{\partial t} = \frac{\partial \bar{P}}{\partial t}, \quad (18)$$

and

$$\bar{\nabla} \cdot \bar{E} = -\frac{1}{\epsilon_0} \bar{\nabla} \cdot \bar{P}. \quad (19)$$

These two equations are still identically satisfied by Eq. (10), provided  $\bar{\Pi}_1$  is a solution of

$$\nabla^2 \bar{\Pi}_1 - \mu \epsilon \frac{\partial^2 \bar{\Pi}_1}{\partial t^2} = -\frac{\bar{P}}{\epsilon}. \quad (20)$$

In a similar manner,  $\bar{\Pi}_2$  can be shown to be a solution of

$$\nabla^2 \bar{\Pi}_2 - \mu \epsilon \frac{\partial^2 \bar{\Pi}_2}{\partial t^2} = -\bar{M}, \quad (21)$$

where  $\bar{M}$  is the magnetization. This equation indicates that  $\bar{\Pi}_2$  has its origin in magnetic dipoles.

Furthermore, the vector potentials  $\bar{\Pi}_1$  and  $\bar{\Pi}_2$  can be derived from the scalar potentials  $\Pi_1$  and  $\Pi_2$  as

$$\Pi_1 = -\bar{\nabla} \cdot \bar{\Pi}_1, \quad (22a)$$

and

$$\Pi_2 = -\bar{\nabla} \cdot \bar{\Pi}_2. \quad (22b)$$

Both  $\Pi_1$  and  $\Pi_2$ , called the Hertz-Debye potentials, are solutions to the scalar wave equation

$$\nabla^2 \Pi - \mu \epsilon \frac{\partial^2 \Pi}{\partial t^2} = 0. \quad (23)$$

Thus, the problem reduces to a solution of Eq. (23) in the appropriate coordinate system. For example, in spherical coordinates the fields can be derived from<sup>30</sup>

$$E_r = \frac{\partial^2(r\Pi_1)}{\partial r^2} + k^2 r\Pi_1, \quad (24a)$$

$$E_\theta = \frac{1}{r} \frac{\partial^2(r\Pi_1)}{\partial r \partial \theta} + \frac{\kappa_2}{r \sin \theta} \frac{\partial(r\Pi_2)}{\partial \phi}, \quad (24b)$$

$$E_\phi = \frac{1}{r \sin \theta} \frac{\partial^2(r\Pi_1)}{\partial r \partial \phi} - \frac{\kappa_2}{r} \frac{\partial(r\Pi_2)}{\partial \theta}, \quad (24c)$$

$$H_r = \frac{\partial^2(r\Pi_2)}{\partial r^2} + k^2 r\Pi_2, \quad (24d)$$

$$H_\theta = -\frac{\kappa_1}{r \sin \theta} \frac{\partial(r\Pi_1)}{\partial \phi} + \frac{1}{r} \frac{\partial^2(r\Pi_2)}{\partial r \partial \theta}, \quad (24e)$$

and

$$H_\phi = \frac{\kappa_1}{r} \frac{\partial(r\Pi_1)}{\partial \theta} + \frac{1}{r \sin \theta} \frac{\partial^2(r\Pi_2)}{\partial r \partial \phi}, \quad (24f)$$

where the propagation constant

$$k^2 = -\kappa_1 \kappa_2 = \omega^2 \epsilon, \quad (25a)$$

with

$$\kappa_1 = i\omega \epsilon, \quad (25b)$$

and

$$\kappa_2 = i\omega. \quad (25c)$$

Since all media are considered to be nonmagnetic,  $\mu$  has been dropped.

For a sinusoidal time dependence,  $e^{i\omega t}$ , the wave equation reduces to

$$\nabla^2 \Pi + k^2 \Pi = 0, \quad (26)$$

where, as before,  $k^2 = \omega^2 \epsilon$ . In spherical coordinates this becomes

$$\frac{1}{r} \frac{\partial^2(r\Pi)}{\partial r^2} + \frac{1}{r^2 \sin \theta} \frac{\partial}{\partial \theta} (\sin \theta \frac{\partial \Pi}{\partial \theta}) + \frac{1}{r^2 \sin^2 \theta} \frac{\partial^2 \Pi}{\partial \phi^2} + k^2 \Pi = 0. \quad (27)$$

The solution to this equation is obtained in the usual manner by the method of separation of variables, i.e., by assuming

$$\Pi = R(r)\Theta(\theta)\Phi(\phi) . \quad (28)$$

The well known, separated, differential equations are

$$\frac{d^2 r R(r)}{dr^2} + [k - \frac{n(n+1)}{r^2}] r R(r) = 0 , \quad (29)$$

$$\frac{1}{\sin\theta} \frac{\partial}{\partial\theta} [\sin\theta \frac{d\Theta(\theta)}{d\theta}] + [n(n+1) - \frac{m^2}{\sin^2\theta}] \Theta(\theta) = 0 , \quad (30)$$

and 
$$\frac{d^2 \Phi(\phi)}{d\phi^2} + m^2 \Phi(\phi) = 0 , \quad (31)$$

where  $n$  is an integer and  $m$  can assume the values  $-n \dots 0 \dots n$ .

The solutions of the radial equation, Eq. (29), are the Ricatti-Bessel functions defined as

$$\psi_n(z) = \left(\frac{\pi z}{2}\right)^{1/2} J_{n+1/2}(z) , \quad (32)$$

and 
$$\chi_n(z) = \left(\frac{\pi z}{2}\right)^{1/2} Y_{n+1/2}(z) , \quad (33)$$

where  $J_{n+1/2}(z)$  and  $Y_{n+1/2}(z)$  are the half-integer order Bessel functions of the first and second kind, respectively, and  $z = kr$  (all function definitions follow Abramowitz and Stegun<sup>32</sup>). Note here that the linear combination

$$\zeta_n(z) = \psi_n(z) - i\chi_n(z) = \left(\frac{\pi z}{2}\right)^{1/2} H_{n+1/2}^{(2)}(z) , \quad (34)$$

where  $H_{n+1/2}^{(2)}(z)$  is the half-integer order Bessel function of the third

kind, is also a solution with the added property of vanishing as  $z \rightarrow \infty$ . From here on  $k_1$  and  $k_2$  will be the propagation constants of medium 1 and 2, respectively, and  $k$  is understood to represent either  $k_1$  or  $k_2$ . The solutions to Eq. (30) are the associated Legendre polynomials

$$\Theta(\theta) = P_n^{(m)}(\cos\theta) . \quad (35)$$

The solutions of Eq. (31) are the common circular functions  $\sin(m\phi)$  and  $\cos(m\phi)$ .

The general solution of the scalar wave equation in spherical coordinates may now be obtained by a linear superposition of all of the particular solutions, each multiplied by a constant coefficient, thus

$$r\Pi = r \sum_{n=0}^{\infty} \sum_{m=-n}^n \Pi_n^{(m)} , \quad (36a)$$

where

$$\Pi_n^{(m)} = [a_n \psi_n(z) + b_n \chi_n(z)] P_n^{(m)}(\cos\theta) [c_n \cos(m\phi) + d_n \sin(m\phi)] . \quad (36b)$$

Due to the discrete boundary at  $r = a$  we know that there is not only the incident field  $(\bar{E}^{(i)}, \bar{H}^{(i)})$  and the internal field  $(\bar{E}^{(w)}, \bar{H}^{(w)})$  but a scattered field  $(\bar{E}^{(s)}, \bar{H}^{(s)})$ . Thus the total electric field in the two regions is written as

$$\bar{E} = \bar{E}^{(i)} + \bar{E}^{(s)} \quad (\text{outside the sphere}), \quad (37a)$$

$$\text{and} \quad \bar{E} = \bar{E}^{(w)} \quad (\text{within the sphere}), \quad (37b)$$

with a similar expression for the magnetic field vector. Thus we must



also have  $\Pi_1^{(s)}, \Pi_2^{(s)}$  and  $\Pi_1^{(w)}, \Pi_2^{(w)}$  as well as  $\Pi_1^{(i)}, \Pi_2^{(i)}$ . The boundary conditions require the tangential components of the electric field and the normal component of the magnetic field be continuous at  $r = a$ . Written in terms of the potentials, these boundary conditions become

$$\frac{\partial}{\partial r} [r(\Pi_1^{(i)} + \Pi_1^{(s)})] = \frac{\partial}{\partial r} [r\Pi_1^{(w)}] , \quad (38a)$$

$$\frac{\partial}{\partial r} [r(\Pi_2^{(i)} + \Pi_2^{(s)})] = \frac{\partial}{\partial r} [r\Pi_2^{(w)}] , \quad (38b)$$

$$im_2^2 k_0 r (\Pi_1^{(i)} + \Pi_1^{(s)}) = im_1^2 k_0 r \Pi_1^{(w)} , \quad (38c)$$

$$\text{and} \quad ik_0 r (\Pi_2^{(i)} + \Pi_2^{(s)}) = ik_0 r \Pi_2^{(w)} , \quad (38d)$$

where  $k_0 = 2\pi/\lambda_0$  is the propagation constant in free space and  $m_1$  and  $m_2$  are the indices of refraction of medium 1 and 2 respectively.

To determine the constants that satisfy these boundary conditions the potentials  $\Pi_1$  and  $\Pi_2$  must be expressed in the form of Eq. (36). To show that this can be done, consider one component of  $\vec{E}^{(i)}$ . The radial component of the incident E-field can be written in spherical coordinates as

$$E_r = e^{ik_2 r \cos\theta} \sin\theta \cos\phi . \quad (39)$$

Substituting Eq. (39) into Eq. (14b) yields

$$e^{ik_2 r \cos\theta} \sin\theta \cos\phi = \frac{\partial^2 (r\Pi_1)}{\partial r^2} + k_2^2 r \Pi_1 . \quad (40)$$

The first factor on the left-hand-side can be written, through the use

of Bauer's formula,<sup>33</sup> as

$$e^{ik_2 r \cos \theta} = \frac{1}{k_2 r} \sum_{n=0}^{\infty} i^n (2n+1) \psi_n(k_2 r) P_n(\cos \theta) . \quad (41)$$

Also 
$$e^{ik_2 r \cos \theta} \sin \theta = - \frac{1}{ik_2 r} \frac{\partial}{\partial \theta} e^{ik_2 r \cos \theta} . \quad (42)$$

Using Eqs. (41), (42) and the identities

$$\frac{\partial}{\partial \theta} P_n(\cos \theta) = - P_n^{(m)}(\cos \theta) , \quad (43)$$

and 
$$P_0^{(1)}(\cos \theta) = 0 , \quad (44)$$

the left-hand-side of Eq. (40) becomes

$$e^{ik_2 r \cos \theta} \sin \theta \cos \phi = \left( \frac{1}{k_2 r} \right) \sum_{n=1}^{\infty} i^{n-1} (2n+1) \psi_n(k_2 r) P_n^{(1)}(\cos \theta) \cos \phi . \quad (45)$$

This result indicates that a solution of the form

$$r\Pi_1 = \frac{1}{k_2^2} \sum_{n=1}^{\infty} \alpha_n \psi_n(k_2 r) P_n^{(1)}(\cos \theta) \cos \phi \quad (46)$$

is needed. Upon substitution of Eqs. (45) and (46) into Eq. (40) and comparing coefficients the relationship

$$\alpha_n [k_2^2 \psi_n(k_2 r) + \frac{\partial^2 \psi_n(k_2 r)}{\partial r^2}] = i^{n-1} (2n+1) \frac{\psi_n(k_2 r)}{r^2} \quad (47)$$

is found. This equation holds if

$$\alpha_n = i^{n-1} \frac{2n+1}{n(n+1)} , \quad (48)$$

since  $\psi_n(kr)$  is itself a solution to Eq. (29). The calculations for the

magnetic potential are similar. Therefore the expressions for the incident fields are

$$r\Pi_1(i) = \frac{1}{k_2^2} \sum_{n=1}^{\infty} i^{n-1} \frac{2n+1}{n(n+1)} \psi_n(k_2 r) P_n^{(1)}(\cos\theta) \cos\phi, \quad (49)$$

$$\text{and } r\Pi_2(i) = \frac{1}{k_2^2} \sum_{n=1}^{\infty} i^{n-1} \frac{2n+1}{n(n+1)} \psi_n(k_2 r) P_n^{(1)}(\cos\theta) \sin\phi. \quad (50)$$

The other potentials expressed in terms of a series expansion of the form of Eqs. (49) and (50) with constant coefficients to be determined are

$$r\Pi_1(s) = -\frac{1}{k_2^2} \sum_{n=1}^{\infty} i^{n-1} \frac{2n+1}{n(n+1)} a_n \zeta_n(k_2 r) P_n^{(1)}(\cos\theta) \cos\phi, \quad (51)$$

$$r\Pi_2(s) = -\frac{1}{k_2^2} \sum_{n=1}^{\infty} i^{n-1} \frac{2n+1}{n(n+1)} b_n \zeta_n(k_2 r) P_n^{(1)}(\cos\theta) \sin\phi, \quad (52)$$

$$r\Pi_1(w) = \frac{1}{k_1^2} \sum_{n=1}^{\infty} i^{n-1} \frac{2n+1}{n(n+1)} c_n \psi_n(k_1 r) P_n^{(1)}(\cos\theta) \cos\phi, \quad (53)$$

$$\text{and } r\Pi_2(w) = \frac{1}{k_1^2} \sum_{n=1}^{\infty} i^{n-1} \frac{2n+1}{n(n+1)} d_n \psi_n(k_1 r) P_n^{(1)}(\cos\theta) \sin\phi. \quad (54)$$

Only the function  $\zeta_n(k_2 r)$  was used for the scattered wave because it has the property of vanishing at infinity. Also, only  $\psi_n(k_1 r)$  was used for the internal wave because  $\chi_n(k_1 r)$  becomes infinite at the origin.

Since the terms in the series expansions are independent of each other, the boundary conditions Eqs. (38a)-(38d) must hold for each corresponding term in the series. This fact leads to a set of four linear equations relating the coefficients  $a_n, b_n, c_n$  and  $d_n$ . These are

$$m[\psi_n'(k_2 a) - a_n \zeta_n'(k_2 a)] = c_n \psi_n'(k_1 a), \quad (55a)$$

$$m[\psi_n'(k_2a) - b_n \zeta_n'(k_2a)] = d_n \psi_n'(k_1a) , \quad (55b)$$

$$\psi_n(k_2a) - a_n \zeta_n(k_2a) = c_n \psi_n(k_1a) , \quad (55c)$$

and 
$$m^2[\psi_n(k_2a) - b_n \zeta_n(k_2a)] = d_n \psi_n(k_1a) . \quad (55d)$$

Here  $m$  is the relative refractive index  $k_1/k_2$  and prime denotes differentiation with respect to arguments.

These equations can now be solved for the coefficients. Since the scattered field is of interest only the results for  $a_n$  and  $b_n$  are needed and are given by

$$a_n = \frac{\psi_n(\alpha) \psi_n'(\beta) - m \psi_n(\beta) \psi_n'(\alpha)}{\zeta_n(\alpha) \psi_n'(\beta) - m \psi_n(\beta) \zeta_n'(\alpha)} , \quad (56)$$

and 
$$b_n = \frac{m \psi_n(\alpha) \psi_n'(\beta) - \psi_n(\beta) \psi_n'(\alpha)}{m \zeta_n(\alpha) \psi_n'(\beta) - \psi_n(\beta) \zeta_n'(\alpha)} , \quad (57)$$

where  $\alpha = k_2a = 2\pi m_2a/\lambda_0$ ,  $\beta = k_1a = m\alpha$ , and  $\lambda_0$  = wavelength of the incident light in vacuum.

The field vectors can now be obtained from Eq. (24).

### C. Far-field solution

Consider next the scattered field at distances sufficiently far from the particle so that  $k_2 r \gg$  (order of the Ricatti-Bessel functions). Under these conditions the expressions describing the scattered field are somewhat simplified<sup>15</sup> since the Hankel function reduces as follows:

$$\zeta_n(k_2 r) = i^{n+1} e^{-ik_2 r} , \quad (58)$$

and 
$$\zeta'_n(k_2 r) = i^n e^{-ik_2 r} . \quad (59)$$

A further simplification, in the far-field, results from the observation that the scattered wave becomes a transverse wave due to the rapid decay of the longitudinal components. The transverse components of the field vectors decay with  $\lambda/r$  in accordance with the inverse square dependence of a spherical wave upon the radial distance. The radial components fall off as  $(\lambda/r)^2$  so that they may be neglected in the far-field zone.

The final result for the far-field zone is then

$$E_\theta = -\frac{H_\phi}{m_2} = \frac{ie^{-ik_2 r}}{k_2 r} S_2 \cos\phi , \quad (60)$$

and 
$$E_\phi = \frac{H_\theta}{m_2} = -\frac{ie^{-ik_2 r}}{k_2 r} S_1 \sin\phi . \quad (61)$$

In the usual manner we identify the amplitude functions

$$S_1 = \sum_{n=1}^{\infty} \frac{2n+1}{n(n+1)} \left( a_n \pi_n(\cos\theta) + b_n \tau_n(\cos\theta) \right) , \quad (62)$$

and 
$$S_2 = \sum_{n=1}^{\infty} \frac{2n+1}{n(n+1)} \left( a_n \tau_n(\cos\theta) + b_n \pi_n(\cos\theta) \right) , \quad (63)$$

where the angular functions are

$$\pi_n(\cos\theta) = \frac{P_n^{(1)}(\cos\theta)}{\sin\theta} , \quad (64)$$

and

$$\tau_n(\cos\theta) = \frac{dP_n^{(1)}(\cos\theta)}{d\theta} . \quad (65)$$

The energy flow in the scattered wave is

$$S = \frac{1}{2} (E_\theta H_\phi^* - E_\phi H_\theta^*) . \quad (66)$$

The intensity of the scattered radiation polarized in the  $\theta$  and  $\phi$  directions is

$$I_\theta = \frac{\lambda^2}{4\pi^2 r^2} |S_2|^2 \cos^2\phi , \quad (67)$$

and

$$I_\phi = \frac{\lambda^2}{4\pi^2 r^2} |S_1|^2 \sin^2\phi . \quad (68)$$

These components are perpendicular and parallel, respectively, to the scattering plane. This plane contains the incident direction and the direction of the scattered wave.

#### D. Calculation methods

Calculating the Mie-scattering functions given in Eqs. (67) and (68) is not a trivial task. Many schemes have been proposed to avoid the complexities of dealing with Bessel functions of large orders and arguments. Entire publications have been devoted to presenting the results of these calculations or describing new algorithms.<sup>34-39</sup> This section will describe the formulas used for the calculations of the desired functions.

The desired quantity is the intensity of the scattered light,

$$I_{\theta} = \frac{\lambda^2}{4\pi^2 r^2} |S_2|^2 \cos^2 \phi, \quad (69)$$

and

$$I_{\phi} = \frac{\lambda^2}{4\pi^2 r^2} |S_1|^2 \sin^2 \phi. \quad (70)$$

These two components are respectively perpendicular and parallel to the scattering plane. For a given wavelength, in a given scattering plane, and at a constant distance away from the sphere, the intensity is proportional to the scattering functions  $S_1$  and  $S_2$ , which are obtained from

$$S_1 = \sum_{n=1}^{\infty} \frac{2n+1}{n(n+1)} \left( a_n \pi_n(\cos\theta) + b_n \tau_n(\cos\theta) \right), \quad (71)$$

and

$$S_2 = \sum_{n=1}^{\infty} \frac{2n+1}{n(n+1)} \left( a_n \tau_n(\cos\theta) + b_n \pi_n(\cos\theta) \right), \quad (72)$$

where the angular functions are

$$\pi_n(\cos\theta) = \frac{P_n^{(1)}(\cos\theta)}{\sin\theta}, \quad (73)$$

and

$$\tau_n(\cos\theta) = \frac{dP_n^{(1)}(\cos\theta)}{d\theta} . \quad (74)$$

Also the coefficients  $a_n$  and  $b_n$  are found from

$$a_n = \frac{\psi_n(\alpha)\psi'_n(\beta) - m\psi_n(\beta)\psi'_n(\alpha)}{\zeta_n(\alpha)\psi'_n(\beta) - m\psi_n(\beta)\zeta'_n(\alpha)} , \quad (75)$$

and

$$b_n = \frac{m\psi_n(\alpha)\psi'_n(\beta) - \psi_n(\beta)\psi'_n(\alpha)}{m\zeta_n(\alpha)\psi'_n(\beta) - \psi_n(\beta)\zeta'_n(\alpha)} , \quad (76)$$

where  $m = k_1/k_2 = m_1/m_2$  is the relative index of refraction,  $\alpha = k_2 a = 2\pi m_2 a / \lambda_0$ ,  $\lambda_0$  = wavelength of the incident light in vacuum,  $\beta = \alpha m$ , and primes denote differentiation with respect to arguments. The functions

$$\psi_n(\alpha) = \alpha j_n(\alpha) , \quad (77)$$

and

$$\zeta_n(\alpha) = \alpha h_n^{(2)}(\alpha) \quad (78)$$

are the Ricatti-Bessel functions with  $j_n(\alpha)$  and  $h_n^{(2)}(\alpha)$  the ordinary spherical Bessel functions of the first and third kind respectively.

By definition the associated Legendre polynomial

$$P_n^{(1)}(\cos\theta) = -\sin\theta \frac{dP_n(\cos\theta)}{d\cos\theta} . \quad (79)$$

Then by differentiation

$$\frac{dP_n^{(1)}(\cos\theta)}{d\theta} = \cos\theta \pi_n(\cos\theta) - \sin^2\theta \pi'_n(\cos\theta) = \tau_n(\cos\theta) . \quad (80)$$

The recurrence relationship



$$P_n^{(1)}(\cos\theta) = \frac{2n-1}{n-1} \cos\theta P_{n-1}^{(1)}(\cos\theta) - \frac{n}{n-1} P_{n-2}^{(1)}(\cos\theta) \quad (31)$$

was used to find  $\pi_n$  by first making a direct substitution to achieve

$$P_n'(\cos\theta) = \frac{2n-1}{n-1} \cos\theta P_{n-1}'(\cos\theta) - \frac{n}{n-1} P_{n-2}'(\cos\theta), \quad (32)$$

with  $P_0' = 0$  and  $P_1' = 1$ , and then using

$$\pi_n(\cos\theta) = -P_n'(\cos\theta). \quad (33)$$

Also by differentiation

$$P_n''(\cos\theta) = (2n-1)P_{n-1}'(\cos\theta) + P_{n-2}''(\cos\theta), \quad (34)$$

with  $P_0'' = 0$  and  $P_1'' = 0$ , which, through the use of Eq. (30), yields  $\tau_n(\cos\theta)$ . These functions are stable to upward recursion.

The function  $\psi_n(\alpha)$  was a little more difficult to obtain since  $j_n(\alpha)$  is not stable to upward recursion; it grows rapidly with decreasing  $n$  (above the oscillation transition). The method adopted was a combination of that proposed by Carbato and Uretsky<sup>40</sup> and J.C.P. Miller.<sup>41</sup>

To avoid the difficulties with rapidly increasing values during downward recursion it was necessary to calculate the ratio  $r_n = j_{n+1}/j_n$ . The starting point for the downward recursion was chosen to insure accuracy up to the largest value of  $n = N$  needed for convergence of the Mie series and was found from<sup>37</sup>

$$N = \alpha + 4.05\alpha^{1/3} + 2 . \quad (85)$$

Using this value for  $N$  the starting value,  $n = N'$ , for the downward recursion was found from<sup>40</sup>

$$N' = N - \log_2 \epsilon_N \left[ A + \frac{Bu'(2 - u'^2)}{2(1 - u'^2)} \right] , \quad (86)$$

where  $u' = 2/(2n + 1)$ ,  $A = 0.1$ ,  $B = 0.35$ , and  $\epsilon_N = 1 \times 10^{-9}$ . Downward recursion was done on the ratios using the formula

$$r_{n-1} = \frac{\alpha}{2n + 1 - \alpha r_n} , \quad (87)$$

with the initial conditions  $r_{N'} = 1$  and  $r_{N'+1} = 0$ . Recursion was continued until a ratio was reached, say  $r_\lambda$ , which exceeded unity, indicating that the transition line had been passed. At this point the ratio was no longer convenient and a change was made to downward recursion on a function  $F_n$  using the formula

$$F_{n-1} = \frac{2n + 1}{\alpha} F_n - F_{n+1} . \quad (88)$$

The initial conditions here were  $F_{\lambda+1} = r_\lambda$  and  $F_\lambda = 1$ . The recursion was carried out until  $n = 1$ . All the  $F_n$ 's are proportional to the real  $j_n$ 's with proportionality constant

$$p = \frac{j_0}{F_0} , \quad (89)$$

where

$$j_0 = \frac{\sin \alpha}{\alpha} . \quad (90)$$

The real  $j_n$ 's were then found by taking

$$j_n = pF_n \quad (91)$$

up through  $n = \lambda$  and then using the calculated ratios

$$j_{n+1} = r_n j_n \quad (92)$$

for the rest of the terms needed (through  $N'$ ).

The above procedure, although somewhat tedious, was the only advantageous way the Bessel functions could be calculated for the large orders and arguments needed.

The function  $\zeta_n(\alpha)$  was found with the aid of the relationship

$$h_n^{(2)}(\alpha) = j_n(\alpha) - iy_n(\alpha) . \quad (93)$$

The  $y_n$ 's are stable to upward recursion and can be calculated using the relationship

$$y_{n-1}(\alpha) = \frac{(2n+1)}{\alpha} y_n(\alpha) - y_{n-1}(\alpha) , \quad (94)$$

with

$$y_0 = -\frac{\cos \alpha}{\alpha} , \quad (95)$$

and

$$y_{-1} = \frac{\sin \alpha}{\alpha} . \quad (96)$$

The rest of the relationships used were

$$\psi_n(\alpha) = \alpha j_n(\alpha) , \quad (97)$$

$$\zeta_n(\alpha) = \alpha h_n^{(2)}(\alpha) , \quad (98)$$

$$\psi_n'(\alpha) = j_n'(\alpha) + j_n(\alpha) , \quad (99)$$

and 
$$\zeta_n'(\alpha) = \alpha h_n^{(2)}(\alpha) + h_n^{(2)}(\alpha) . \quad (100)$$

With 
$$j_n'(\alpha) = j_{n-1}(\alpha) - \frac{n-1}{\alpha} j_n(\alpha) , \quad (101)$$

and 
$$h_n^{(2)}(\alpha) = h_{n-1}^{(2)}(\alpha) - \frac{n+1}{\alpha} h_n^{(2)}(\alpha) . \quad (102)$$

The Mie-scattering calculations were done on an IBM 4341 computer using the Fortran program which is given in Appendix A. The program was checked for accuracy by comparison to results found in Refs. 12, 13, 26, and 27.

### E. Computational results

For comparison purposes it was convenient to calculate an angular efficiency function or angular "gain" such that

$$G2 = \frac{4|S_2|^2}{\alpha^2} . \quad (103)$$

This "gain" is the ratio of the scattered intensity to the intensity that would be found in any direction if the bubble scattered the entire incident energy isotropically. The parallel component,  $S_2$ , was chosen for these experiments because this component exhibits higher scattering intensities, overall, and the fine structure is less than for the perpendicular component,  $S_1$ .<sup>24</sup>

Figures 2a-d show the  $\log(G2)$  plotted as a function of scattering angle, from 0 to 180 degrees, for a bubble radius of 50  $\mu\text{m}$ . The graph is presented in four parts for added clarity. The parameters used in these calculations are as follows: index of refraction of the air = 1.0, index of refraction of water relative to air = 1.33, relative index  $m = 0.75$ , wavelength  $\lambda_0 = 632.8 \text{ nm}$ . Figure 2a shows the prominent forward scattering, sometimes referred to as the Mie effect.

To demonstrate the sensitivity of the pattern to radius, Fig. 3 shows a plot of  $\log(G2)$  for scattering angles from 30 to 45 degrees for radii of 50  $\mu\text{m}$  and 51  $\mu\text{m}$ . Figure 4 shows  $\log(G2)$  plotted for radii between 50  $\mu\text{m}$  and 75  $\mu\text{m}$  and a scattering angle of 20 degrees and 30 degrees. This graph serves to demonstrate the need to measure accurately the angle to the detector. The choice of angles to be used

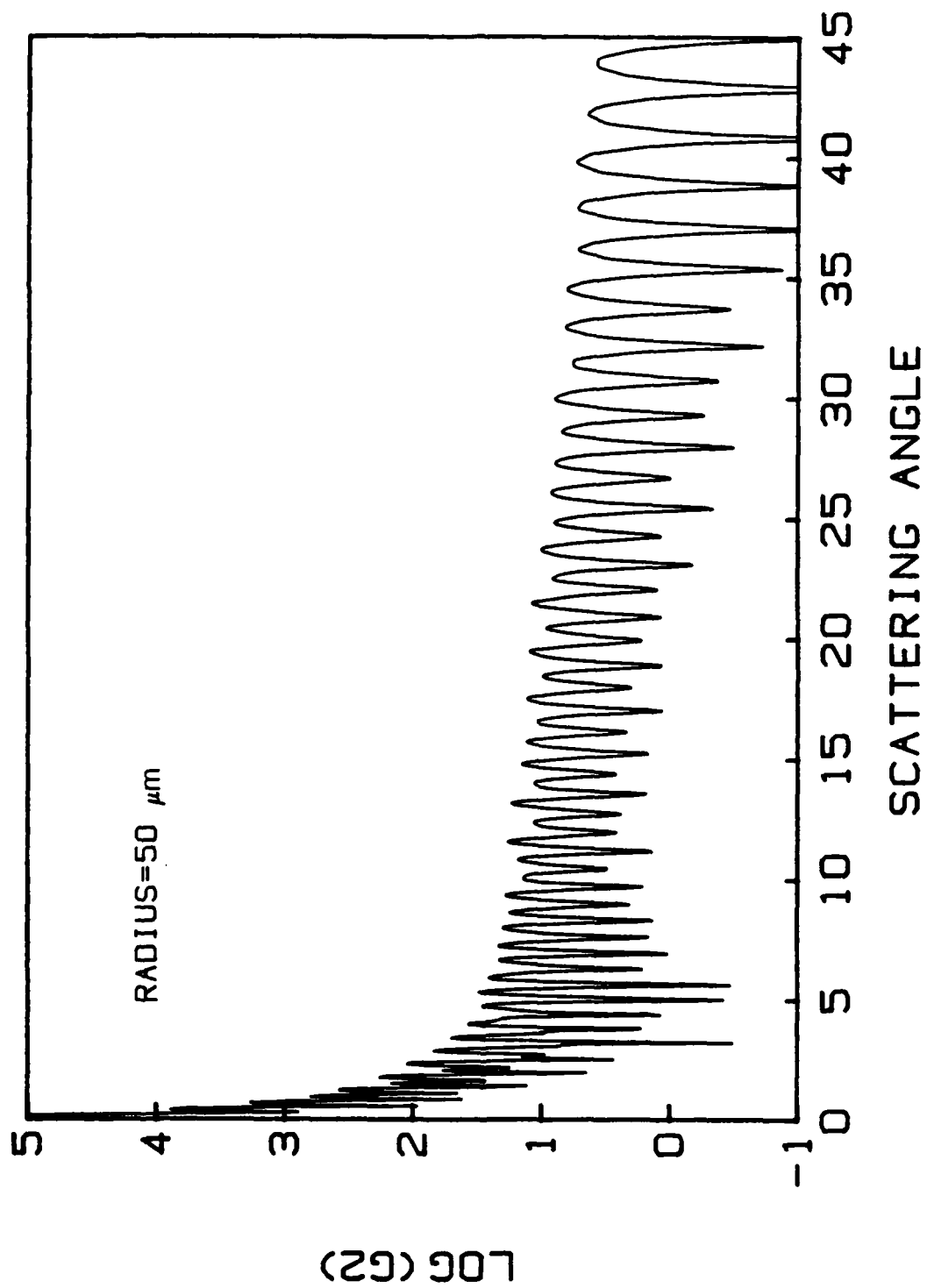


FIG. 2a. Variation of gain with angle, radius = 50 $\mu\text{m}$ .

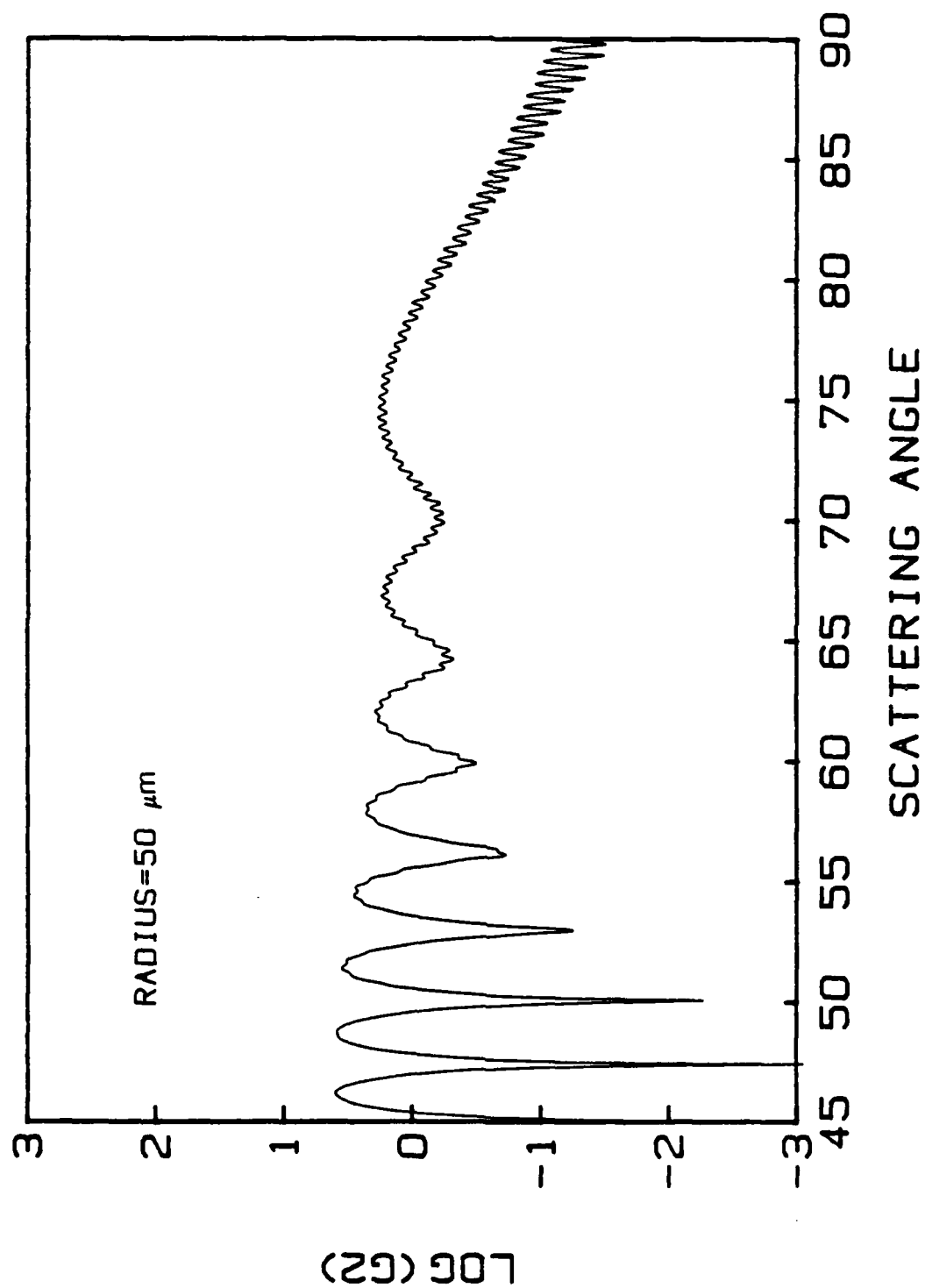


FIG. 2b. Variation of gain with angle, radius = 50 $\mu\text{m}$ .

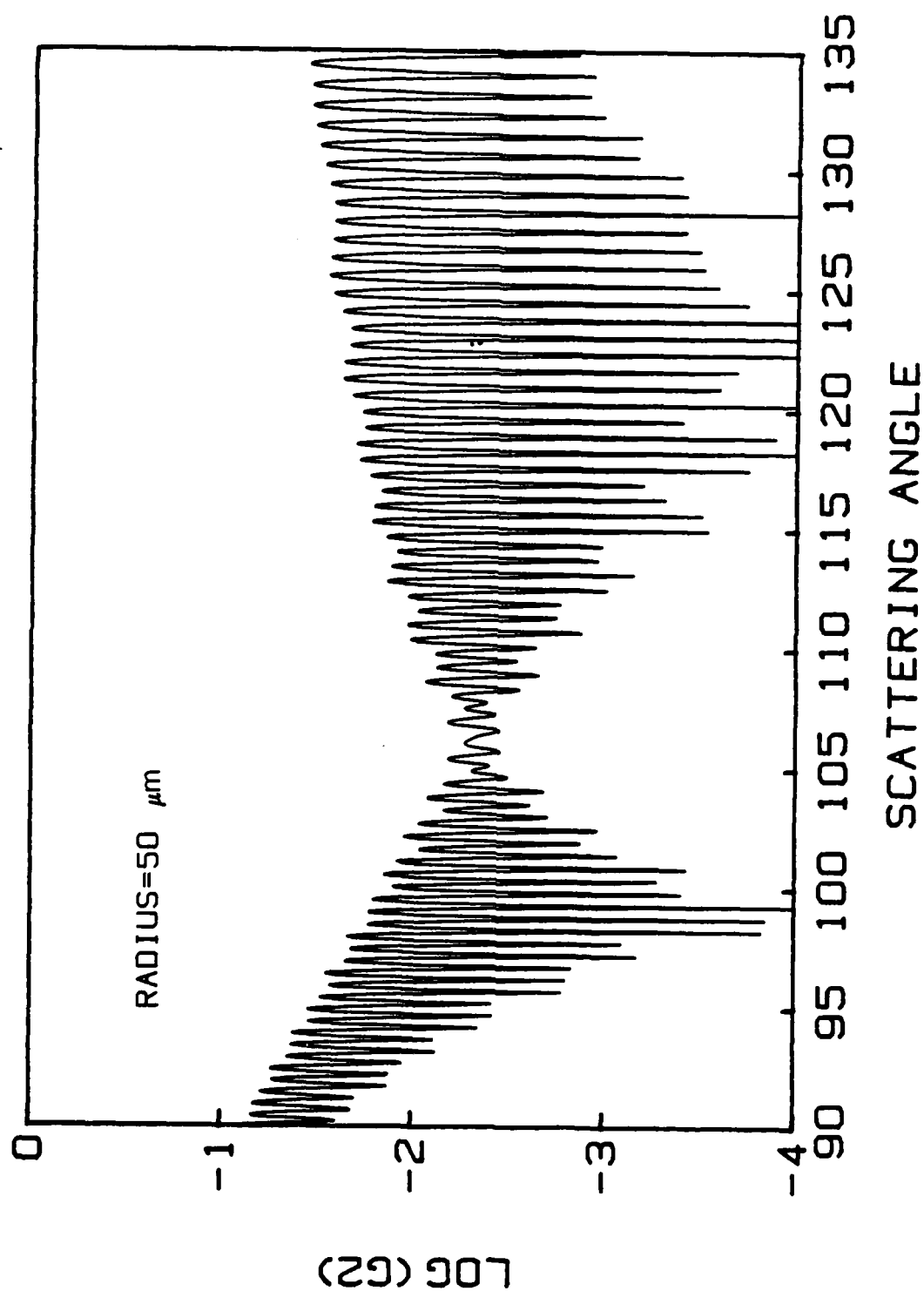


FIG. 2c. Variation of gain with angle, radius = 50μm.



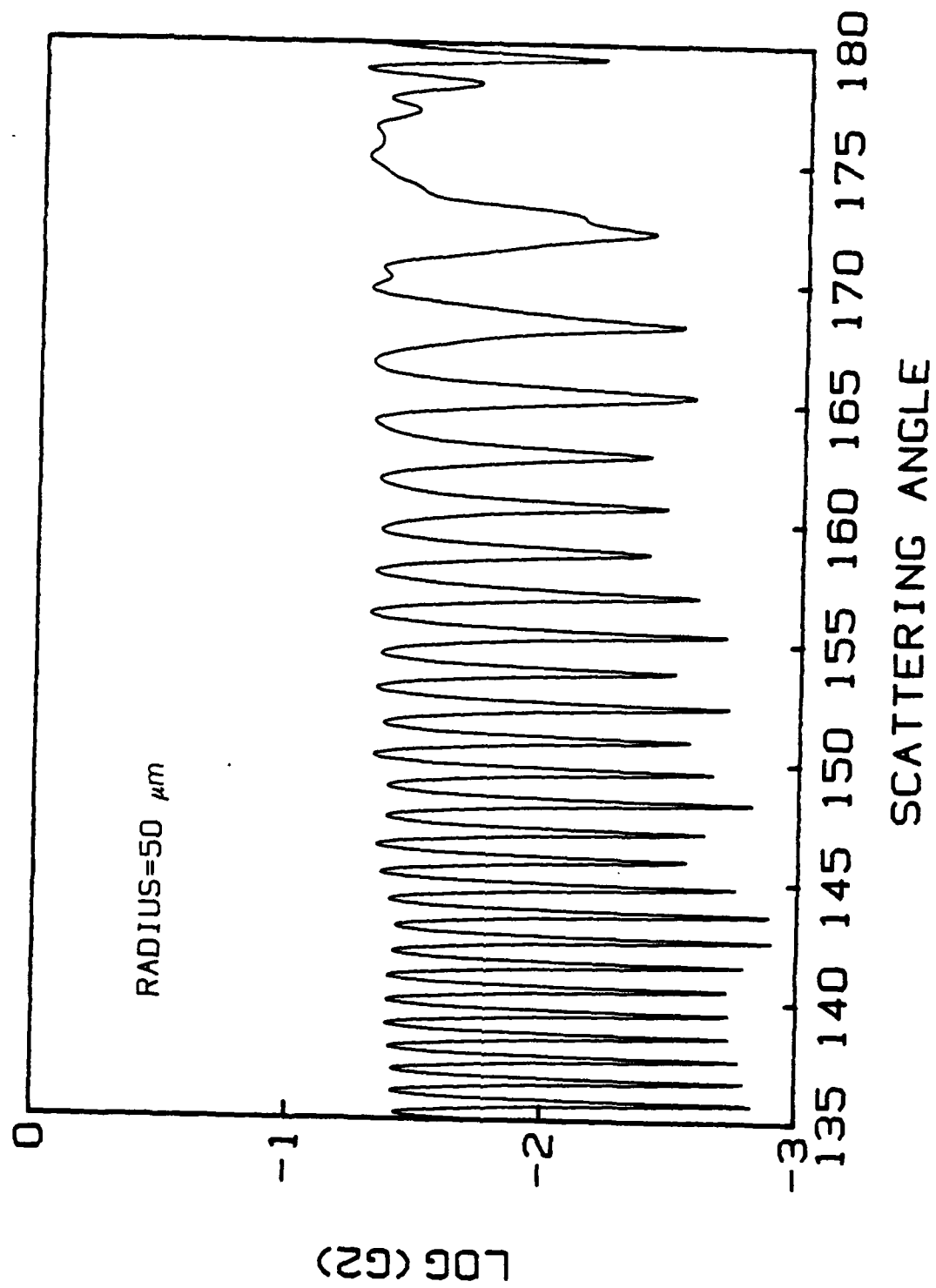


FIG. 2d. Variation of gain with angle, radius = 50 $\mu\text{m}$ .

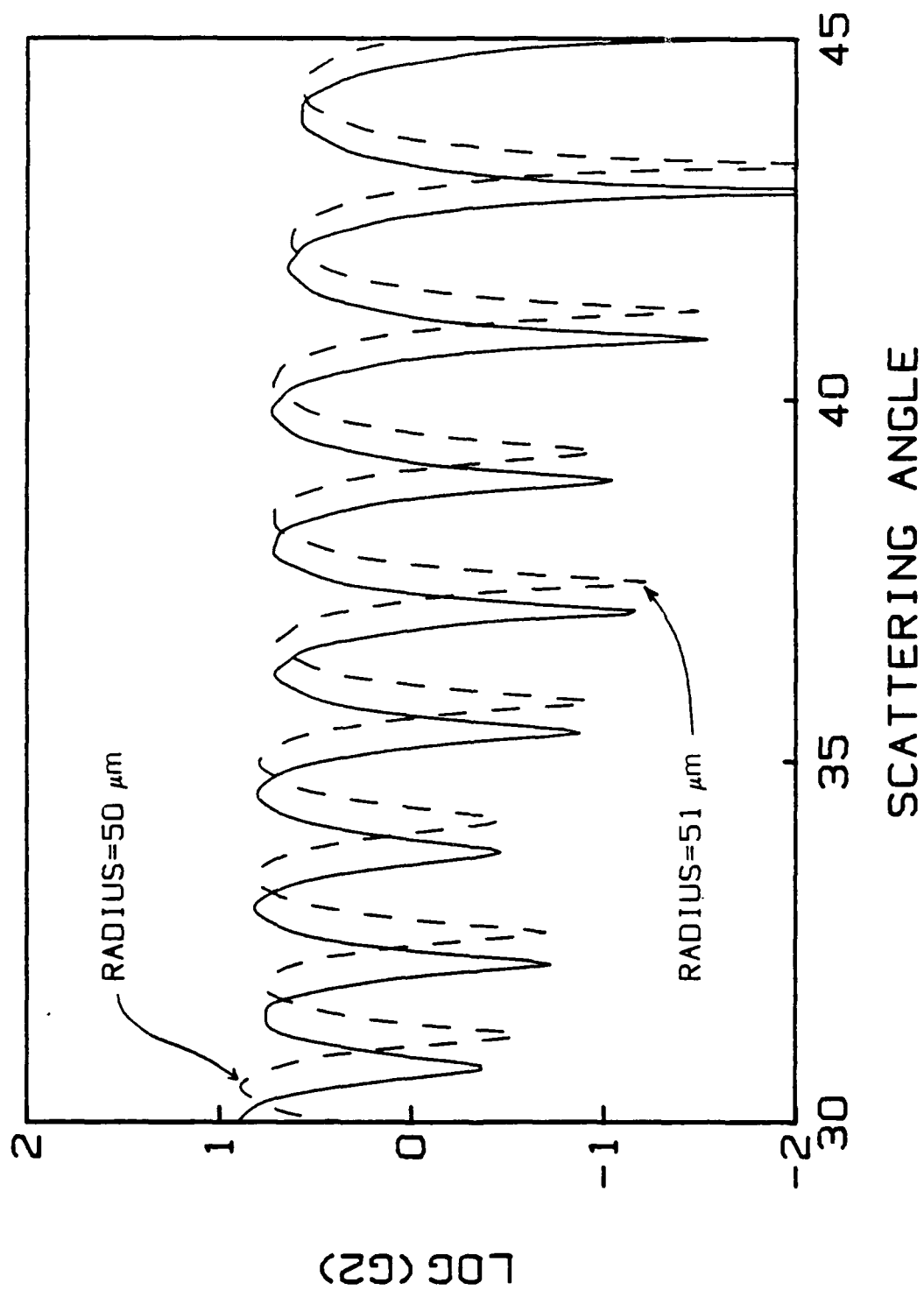


FIG. 3. Variation of gain with angle radius = 50 $\mu\text{m}$  and 51 $\mu\text{m}$ .

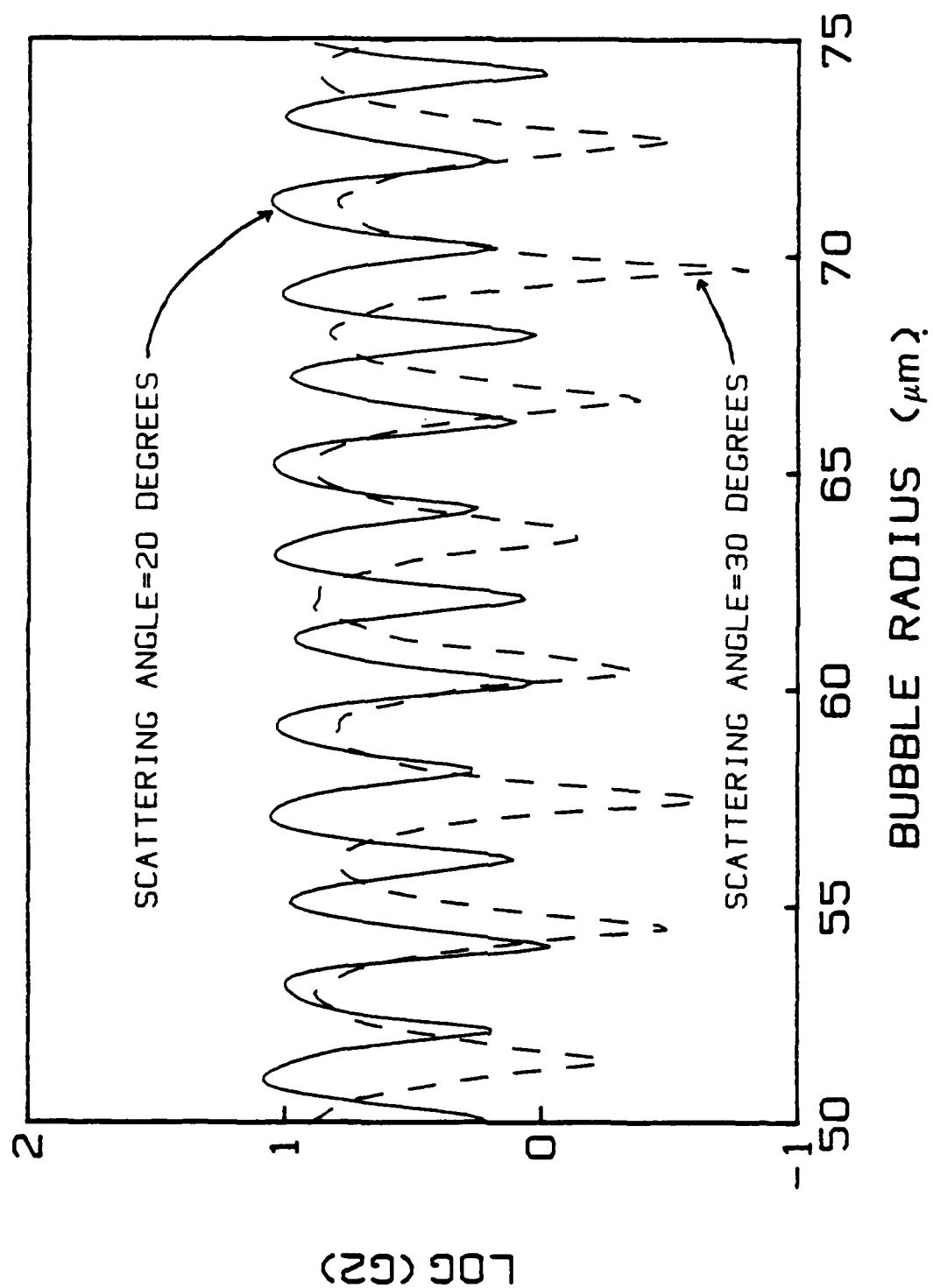


FIG. 4. Variation of gain with radius for scattering angles 20 and 30 degrees.

in the experimental part of this study was based on a desire to obtain as close as possible a one-to-one relationship between scattered intensity and radius. The two angles decided upon have no other special significance. The two angles eventually chosen were 55 degrees and 80 degrees. Two angles were selected so that the 55 degree data could supply an initial calibration for the 80 degree data. Shown in Fig. 5 is a graph of the relative intensity as a function of radius from 20  $\mu\text{m}$  to 100  $\mu\text{m}$  for a scattering angle of 55 degrees. This angle was chosen because of the separation of the peaks and the relative smoothness of the fine structure. Figure 6 shows a similar graph for a scattering angle of 80 degrees. The overall shape of this graph is desirable in that the intensity rises fairly regularly (ignoring fine structure) with radius.

In the initial experimental arrangement a large aperture (see Sec. II, Part A.) was used to permit a rough trial. With this aperture in place an unexpected shape was found in the data at 55 degrees (see Fig. 14), in that the low intensity points had a larger amplitude than was predicted in Fig. 5. In considering the possible reasons for this occurrence, it was realized that with a large aperture the photodiode pickup was seeing more than just a small angle around 55 degrees ( $55 \pm .07$  degrees). Subsequent calculation of the acceptance angle for this aperture (1.6 mm) gave 2 degrees. A numerical integration was then conducted for scattering angles from 54 to 56 degrees. The trapezoidal method was employed with a 0.2 degree step size. The results of these calculations are shown in Fig. 7. The desired shape was present with the

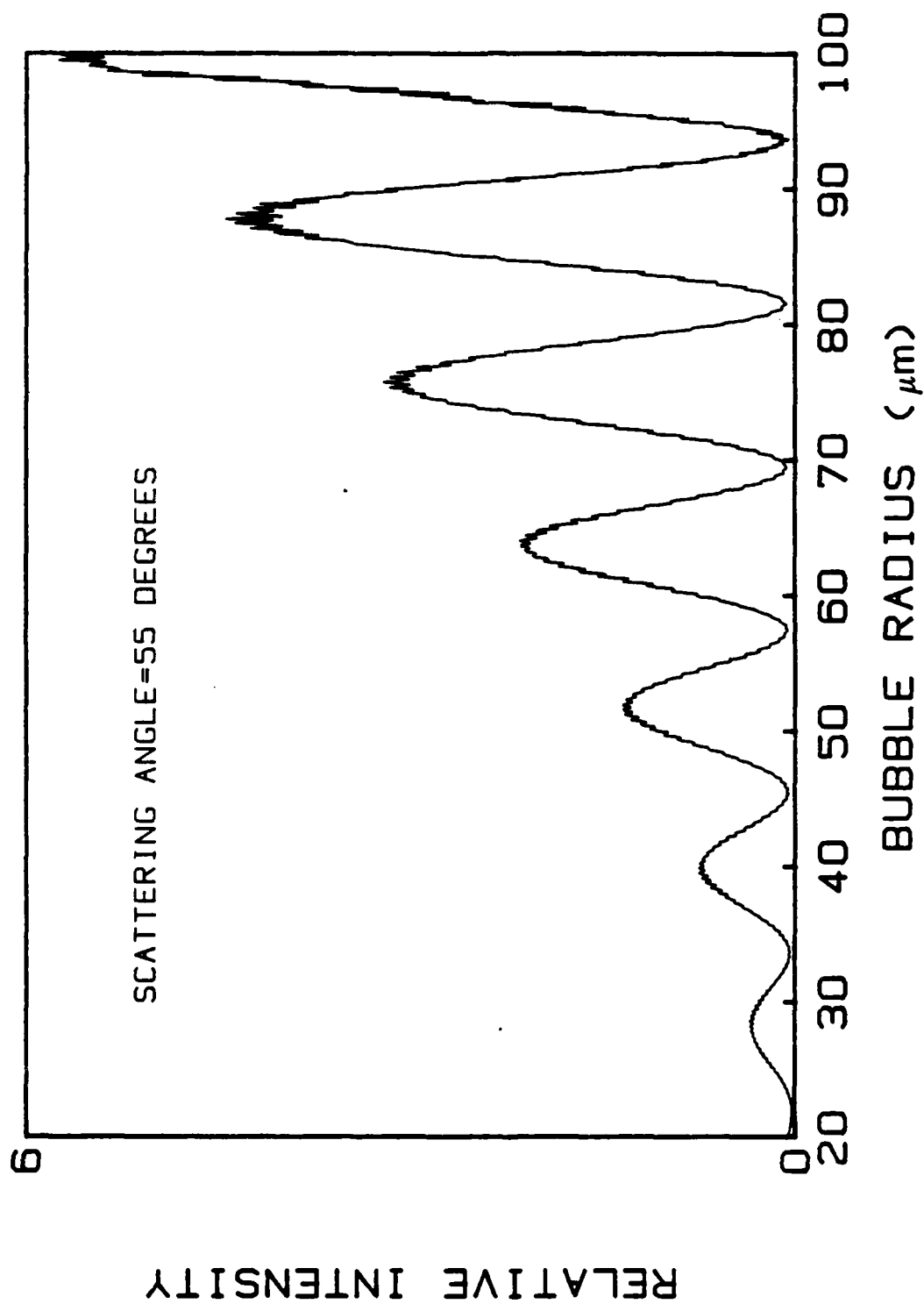


FIG. 5. Relative intensity as a function of radius at a scattering angle of 55 degrees.

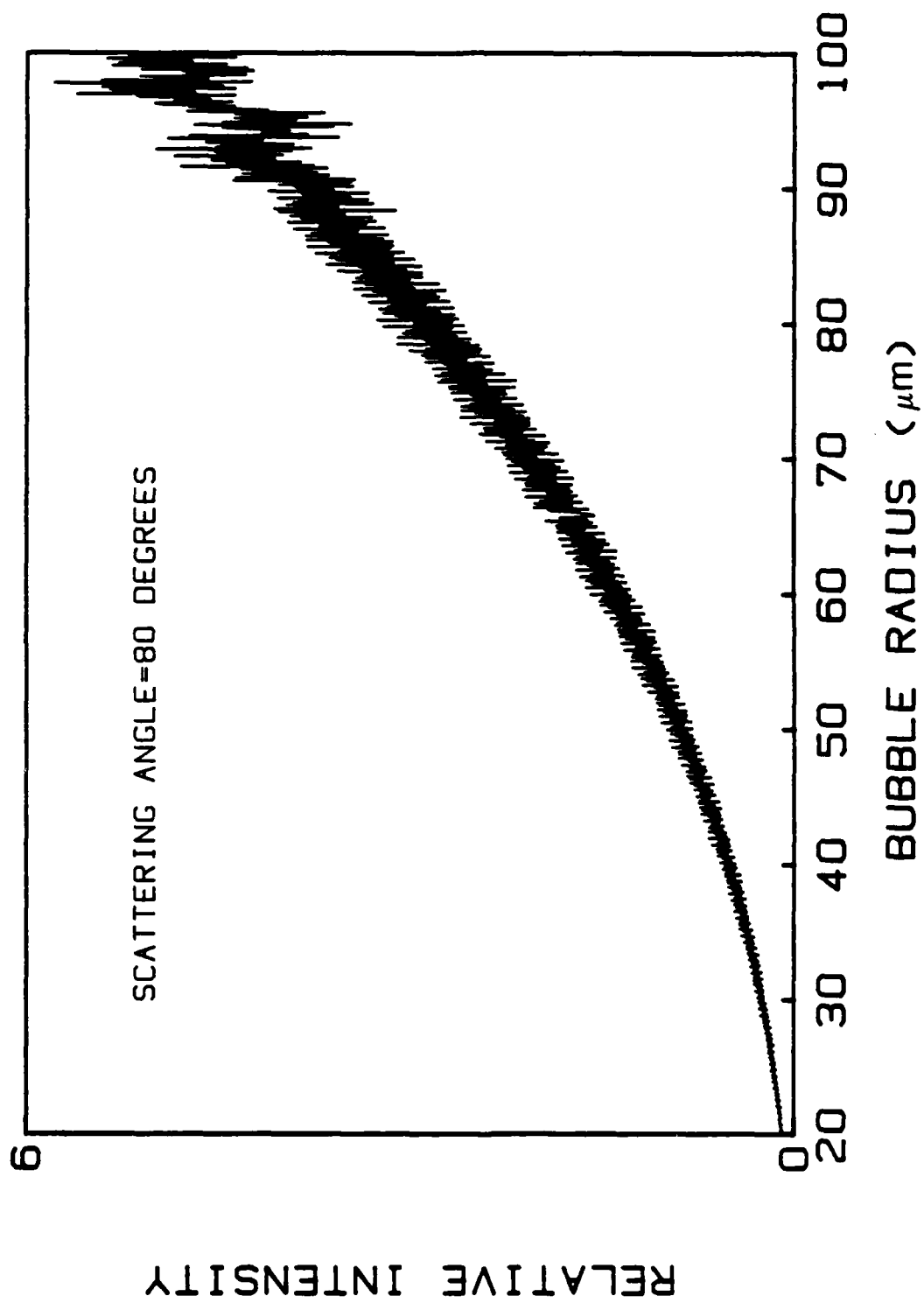


FIG. 6. Relative intensity as a function of radius at a scattering angle of 80 degrees.

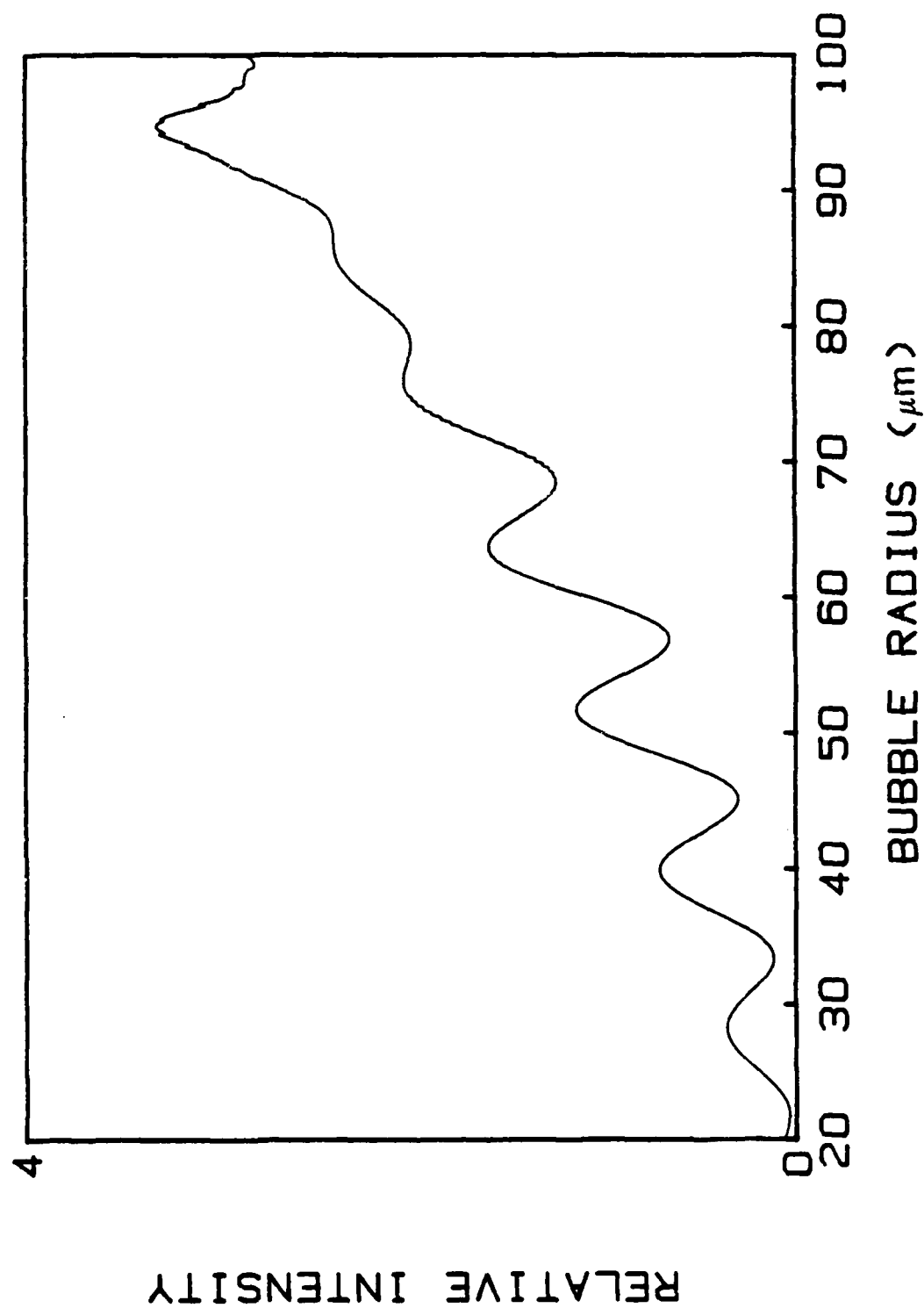


FIG. 7. Results of numerical integration of intensity from 54 to 56 degrees as a function of radius.

added feature of reduced fine structure. Similar calculations were conducted for 79 to 81 degrees with a step size of 0.1 degrees. The results of these calculation are shown in Fig. 8. The almost total elimination of fine structure was observed.

A functional dependence was needed to use the light intensity at 80 degrees as a direct measure of the radius. A least squares fit was done on the intensity data for radii from 20  $\mu\text{m}$  to 100  $\mu\text{m}$  for the integrated results at 80 degrees. The functional dependence for this angle was

$$\text{Radius} = 50.1(\text{Relative Intensity})^{.404}, \quad (104)$$

with a goodness of fit of 99.994%.



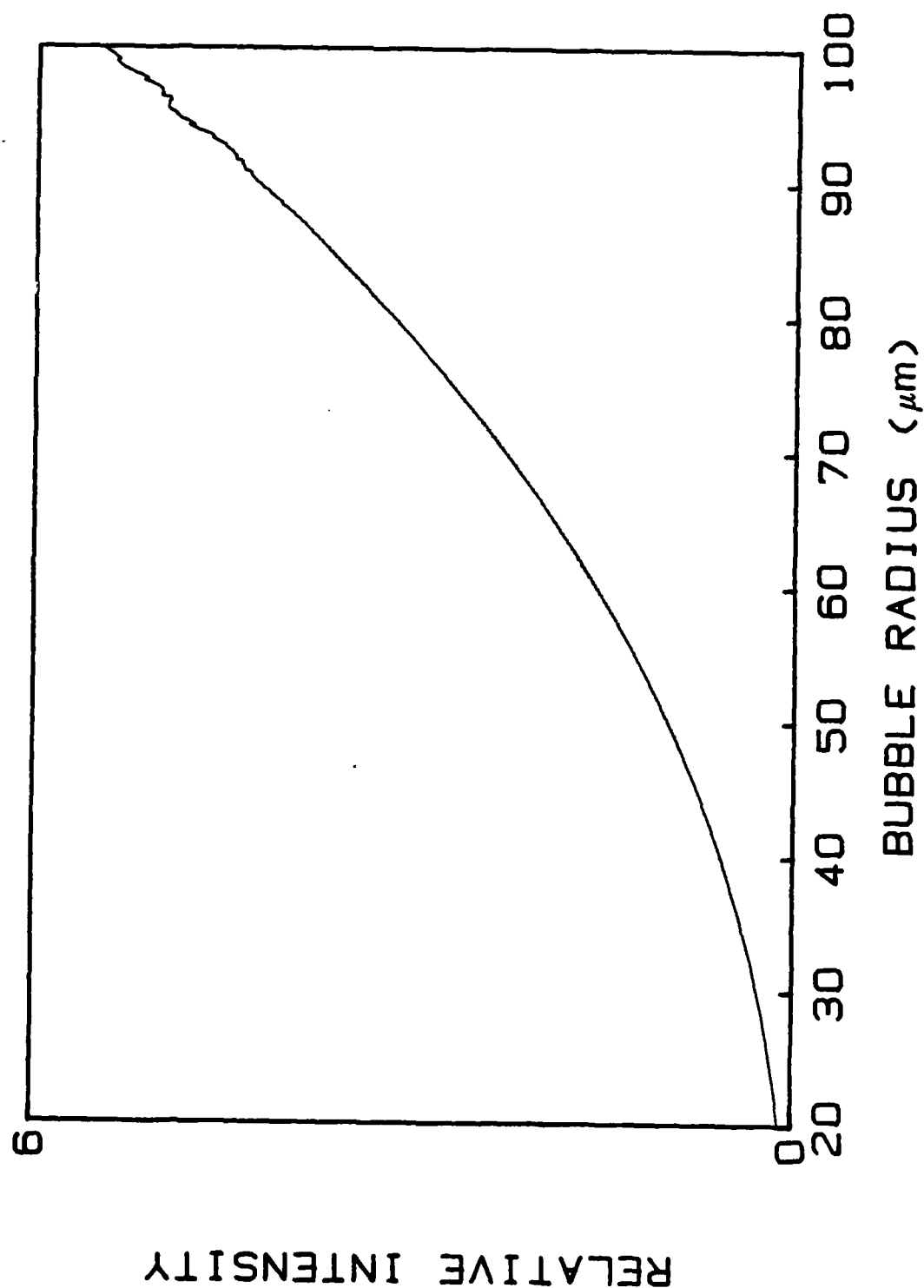


FIG. 8. Results of numerical integration of intensity from 79 to 81 degrees as a function of radius.

## II. EXPERIMENTAL

### A. Apparatus

A block diagram of the experimental setup is shown in Fig. 9. The main components were a 7-mW He-Ne laser, a cylindrical acoustic levitation cell, and a photodiode. In addition there were some non-specialized items such as the photodiode bias supply and amplifier, and the cell's driving oscillator and amplifier. Data was taken and analysed with a Cyborg Corporation ISAAC model 91A data acquisition system/Apple II computer combination.

The He-Ne laser was a model LT-7P manufactured by Aerotech, Incorporated, providing 7-mW minimum output power at 632.8 nm in the TEM<sub>00</sub> mode. There was a 500:1 linear polarization factor and a  $1/e^2$  beam width of 1.0 mm. The beam profile is shown in Fig. 10. The laser was mounted so that the E-field was parallel to the scattering plane (the scattering plane was chosen to be parallel to the floor) and the beam traversed the vertical center of the photodiode suspension plate.

The cylindrical cell, Fig. 11, consisted of two ceramic transducers separated by a vertical length of glass. The cell was closed at the bottom and filled with filtered, distilled water. The transducers were driven in one of their resonant modes at a frequency around 22 kHz.

The photodiode was an RCA device # C30957E with a responsivity of 0.4 A/W at 632.8 nm. The photodiode circuit used is shown in Fig. 12. When radiant flux is absorbed in the reverse-biased photodiode, the

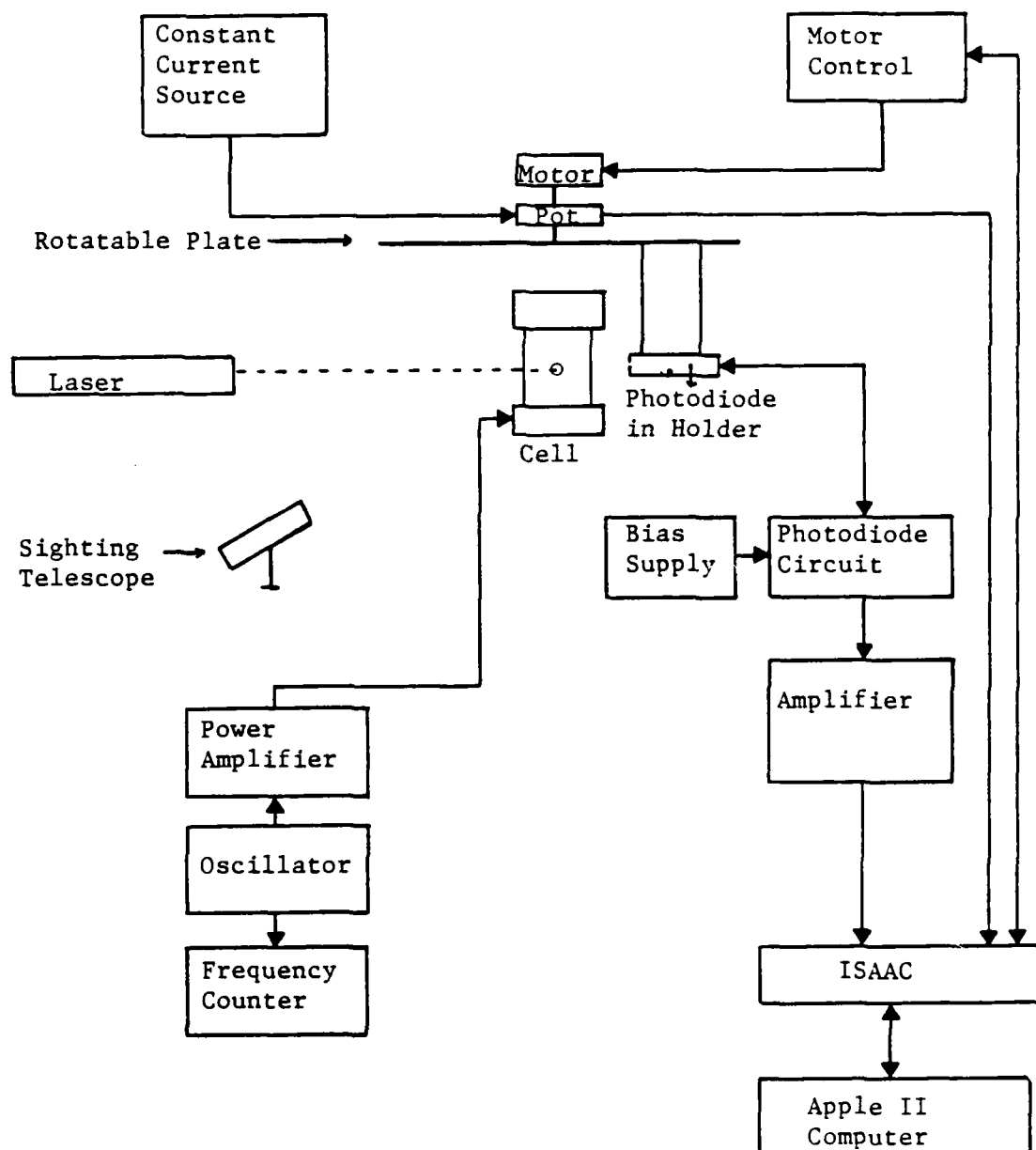


FIG. 9. Block diagram of experimental setup.

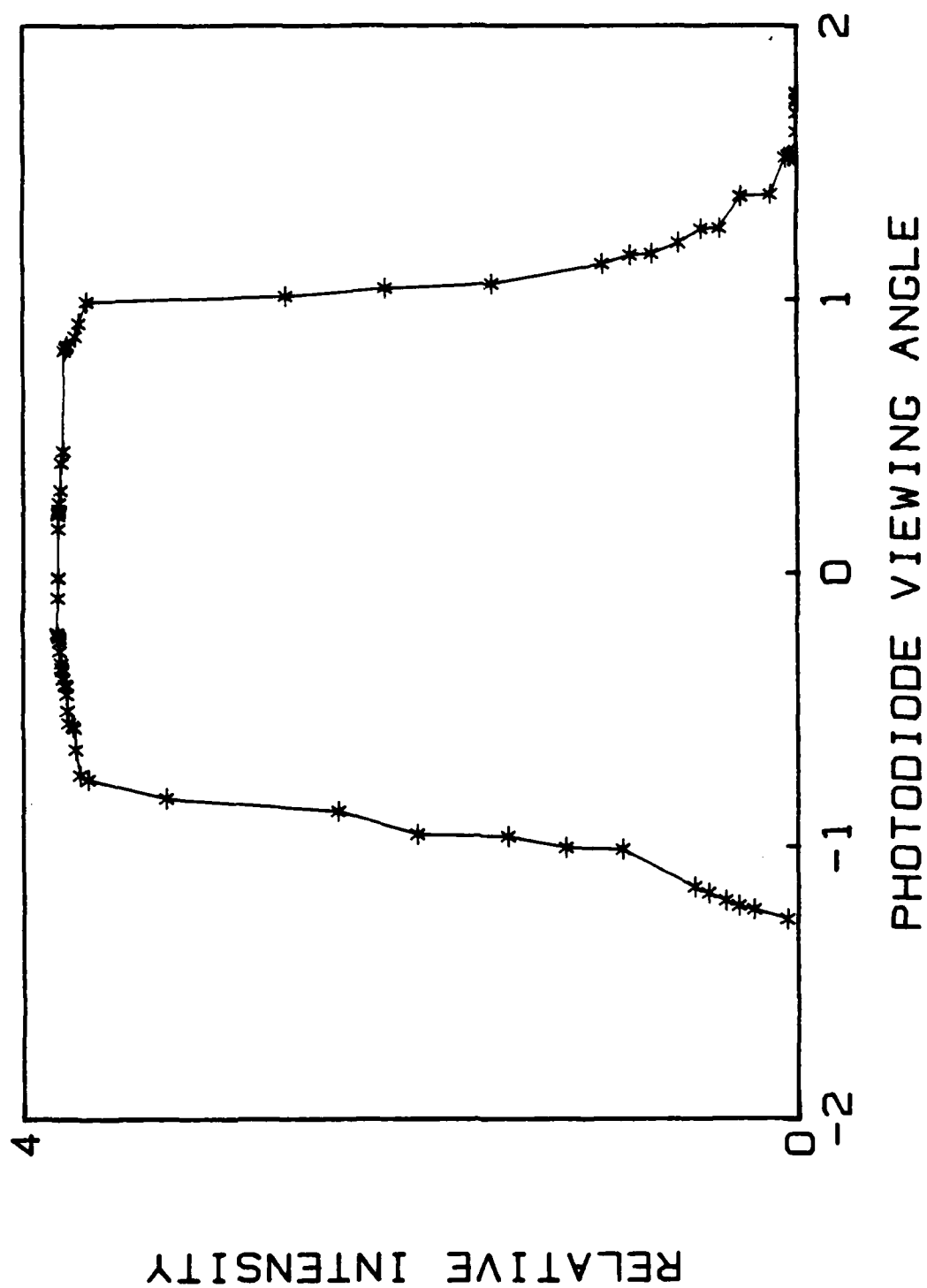


FIG. 10. Laser beam profile taken with 1.6 mm aperture.

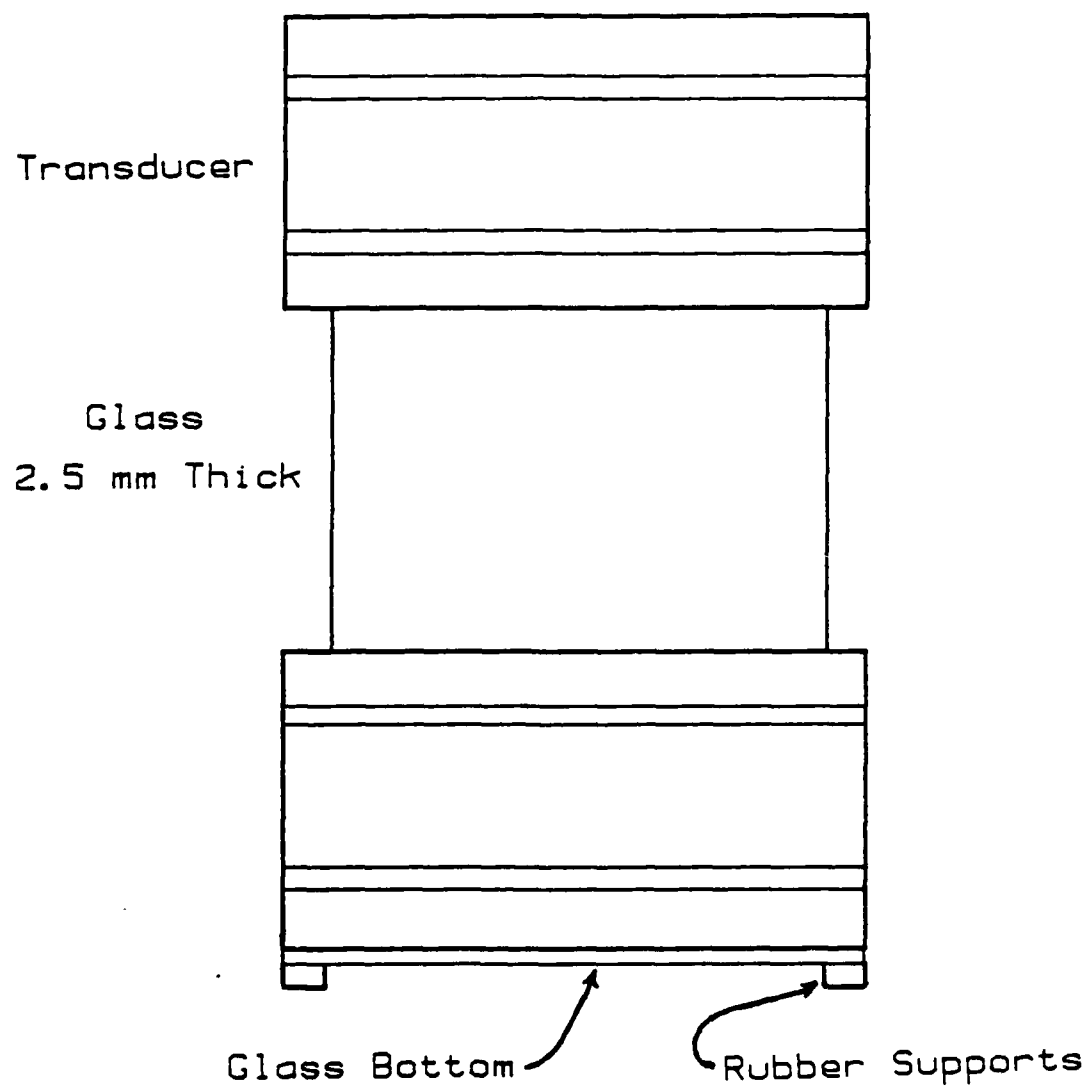


FIG. 11. Scale drawing (1:1) of the acoustic levitation cell.

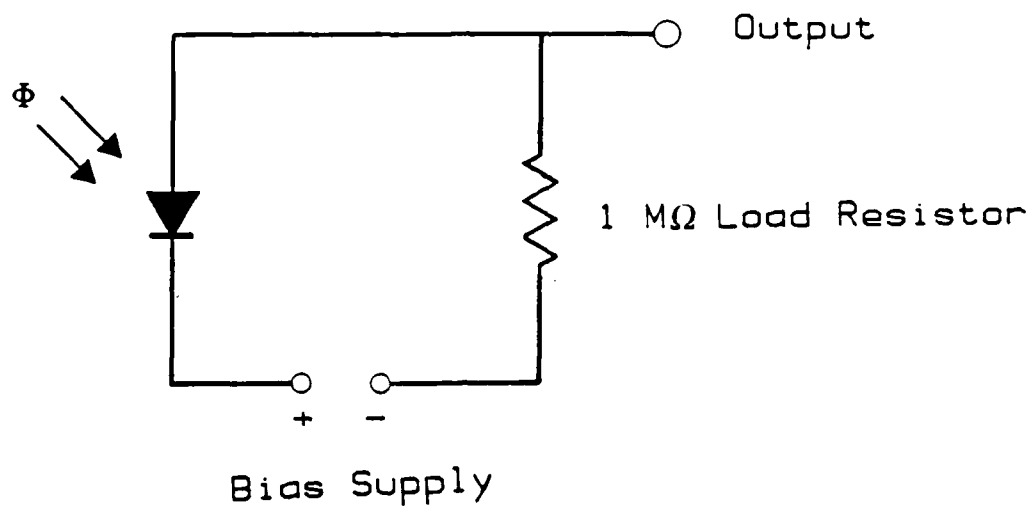


FIG. 12. Photodiode circuit

electric field sweeps the created electron-hole pair out of the depletion region. The resulting photocurrent was used to develop a voltage across the external one Megaohm resistor. This voltage, which was proportional to the intensity of the incident flux, was then amplified by a high input impedance DC amplifier, the output of which was fed into the data acquisition system.

The photodiode was mounted in a custom built holder that allowed for the control of the acceptance angle. The holder was designed to have interchangeable apertures ranging down to 0.1 mm diameter for an acceptance angle of 0.13 degrees. The holder was suspended from a horizontally mounted circular plate. The center of this plate was attached to a voltage divider circuit. The voltage divider consisted of a precision, linear potentiometer which was fed by a constant current source. The pickoff voltage from this potentiometer was calibrated to provide angular information. The potentiometer-plate combination was attached to a motor which was used to give angular sweeps.

## B. Procedure

Since the scattered light intensity was critically dependent on the scattering angle an accurate determination of the photodiode angle was essential. This task was undertaken as the first step in the experiment. The zero scattering angle was defined as forward and was determined from a weighted average over the beam profile of the kind shown in Fig. 10. The beam profile was obtained by stepping the photodiode, with the motor, from one side of the beam to the other, voltage readings being taken at each step. The profile shown in Fig. 10 was taken with the 1.6 mm aperture in place. Two independent methods were then used to determine the correlation between potentiometer voltage and scattering angle. The first method consisted of mounting a spectrometer at the vertical center of the photodiode suspension plate. The telescope of the spectrometer was then used to sight the angles. The potentiometer voltage for each angle was read from a digital volt meter and the correlation was made by a least squares fit from several angles. The second method consisted of mounting a diffraction grating on the spectrometer, shining the laser through the grating, and scanning the photodiode through the pattern. Matching the measured locations of the peaks to the angles given by theory gave the relationship between angle and voltage. The two methods agreed to within 0.8% and provided angular information accurate to within 0.25 degrees. A test of the relationship was made by mounting a diffraction slit in place of the grating. The results of one of these scans is presented in Fig. 13



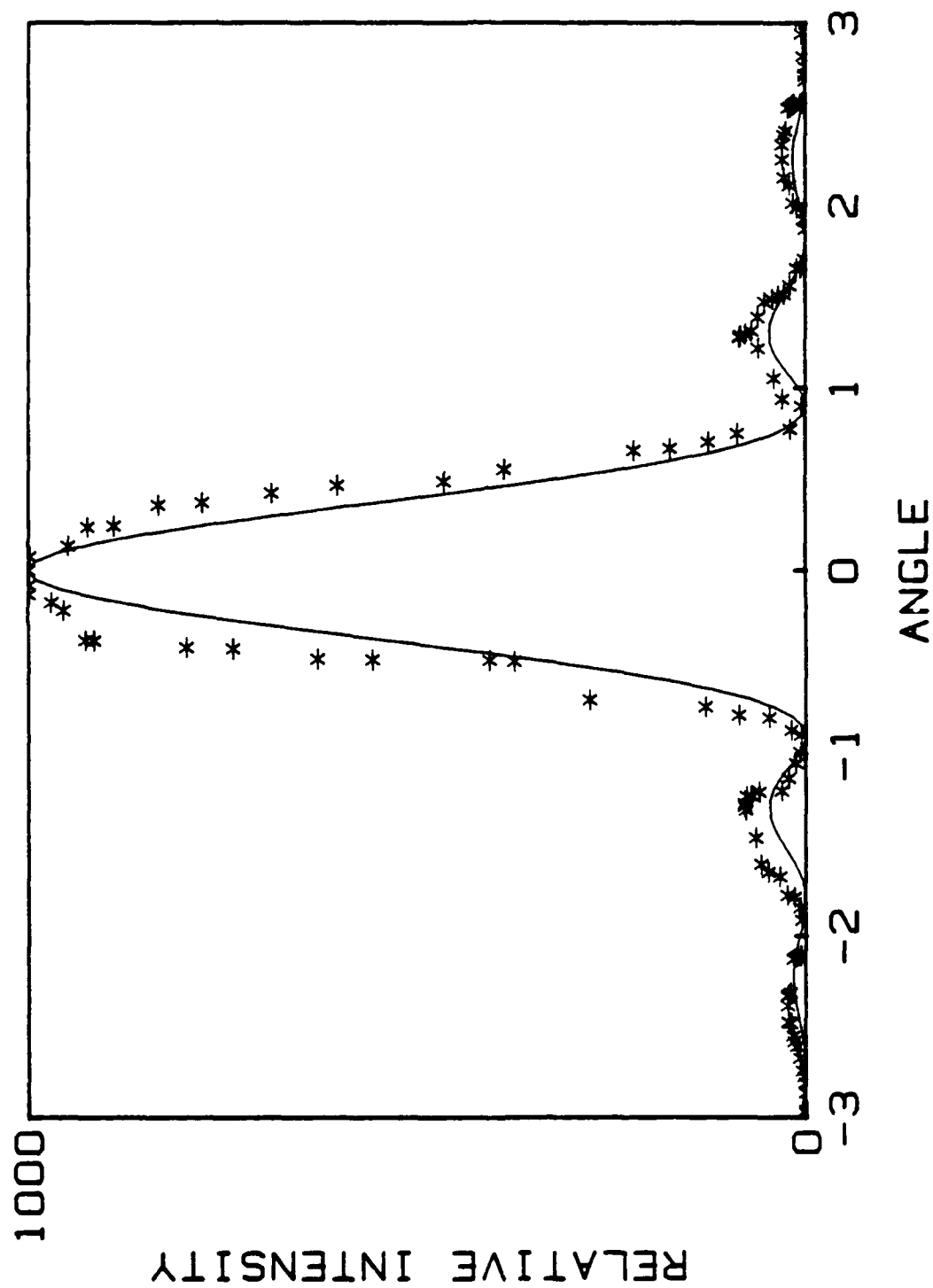


FIG. 13. Experimental points and theoretical curve of .04mm single slit diffraction pattern.

along with the theoretical pattern for the given slit width.

The levitation cell was then set in place and aligned to be in the vertical center of the plate. A standing wave acoustic field was established in the cell such that an antinode existed in the center. This was achieved by varying the water level in the cell as well as the frequency. The radiation force on the bubble, in the center of the cell, was then used to balance the buoyancy force and effectively "levitate" the bubble, causing it to remain relatively stationary. Bubbles were initially induced in the cell by increasing the pressure amplitude until gaseous cavitation occurred and then reducing the amplitude to allow for coalescence into a single bubble. This levitation technique also allowed for the adjustment of the bubble position up and down, through a slight variation of the acoustic-pressure amplitude.

The voltage corresponding to the light intensity was obtained as follows: With the photodiode set at the desired angle the position of the bubble was adjusted until the bubble was in the center of the laser beam. The ISAAC/Apple was then triggered, manually, to take the voltage readings (100 readings/data point). The background voltage was then subtracted from this reading.

The rise-velocity radius was obtained by using a sighting telescope that had graduated graticule marks. The actual distance that the bubble traveled was known in relationship to these marks. With the bubble "levitated" in the center of the field-of-view of the telescope the sound field was turned off, simultaneously, a timer was turned on. The bubble was allowed to rise a few marks, the timer was stopped and the

sound field turned back on. The time and distance of the rise gave the rise-velocity, assuming negligible time to reach terminal velocity.<sup>29</sup> The radius was then determined through an iterative calculation.

Little time was allowed to elapse between the light intensity reading and the rise-velocity determination. This was done in an attempt to assure that the radius did not change significantly between the two methods, since bubbles between 20  $\mu\text{m}$  and 80  $\mu\text{m}$  change size at a rate on the order of 0.3  $\mu\text{m/s}$  in low amplitude sound fields.<sup>11</sup>

For consistency and accuracy certain procedures were always followed. First, the photodiode readings were triggered only when the bubble was in a specified location, as viewed through the sighting telescope. Second, the rise time for bubbles was kept between one and two seconds whenever possible. Times less than one second showed reaction time errors which were noticeable in the large-bubble data scatter (see Fig. 16). Times greater than two seconds allowed the bubble to dissolve too much. This effect was more prevalent in smaller bubbles. A 20  $\mu\text{m}$  bubble was observed to dissolve in approximately 10 seconds. Third, attempts were made to avoid parallax errors in noting rise distances.

The water was distilled and filtered through a 7  $\mu\text{m}$  filter to eliminate as many background scatterers as possible. The water used was also slightly degassed to reduce growth rates. The glass opposite the photodiode and at zero degrees was covered (inside the cylinder) with black tape to reduce reflections. Experiments were conducted with the room lights off and each run was limited to 100 data points to reduce

the fatigue error, which increased reaction time.

### C. Results

The photodiode was positioned at 55 degrees and rise-velocity and light scattering intensity data were taken (1.6 mm aperture used). The raw values for light intensity were divided by the value which was achieved for a rise-velocity radius of 50  $\mu\text{m}$ . The cumulative results are given in Fig. 14. These data match that of the theoretical predictions of Fig. 7 except for a shift in radius. The spread of the data points was an indication of the error and error bars of one standard deviation are also presented. When the theoretical results and the data were compared it was found that the rise-velocity method gave values for the radius that were 10% too small. Figure 15 shows this. In this figure the value of the rise-velocity radius at 51.7  $\mu\text{m}$  was forced to match the value of the theoretical curve at 56.9  $\mu\text{m}$ . This same 10% shift in radii was carried through for the rest of the experimental rise-velocity values. A correction was also made for the shift in relative intensity due to the initial error in radius. The match of the data with the theory indicated that this was indeed the correct shift. Since the form of the drag law is not linear the actual shift of all radii may not be 10% but the overall fit indicated that this was a good first approximation.

Similar measurements were made with the photodiode shifted to 80 degrees. The same 10% shift in the rise-velocity method radii was used; the data are plotted along with the theory in Fig. 16. Again, the match indicates that this shift was real.

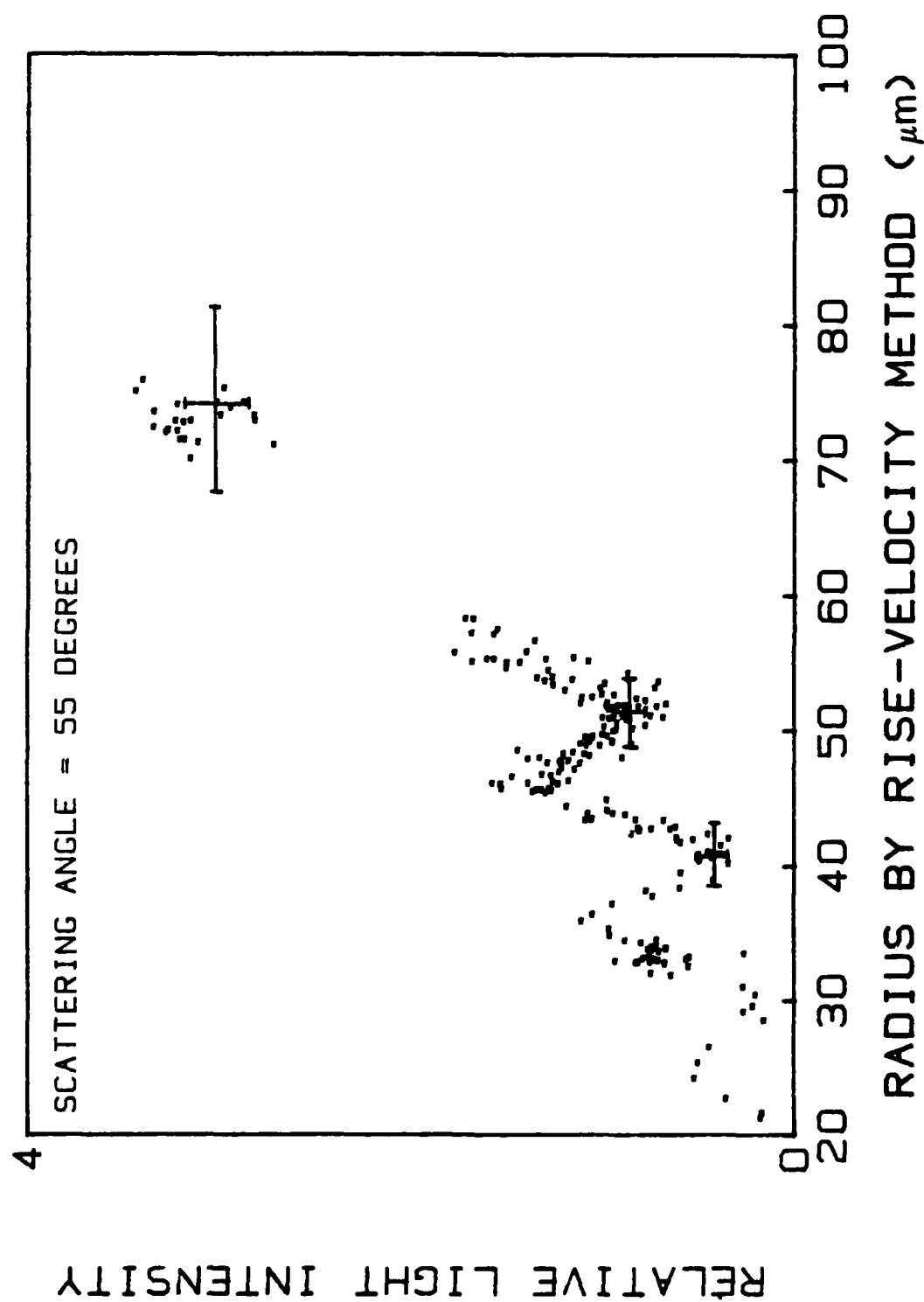


FIG. 14. Light intensity from bubbles as a function of radius obtained by rise-velocity method, scattering angle = 55 degrees.

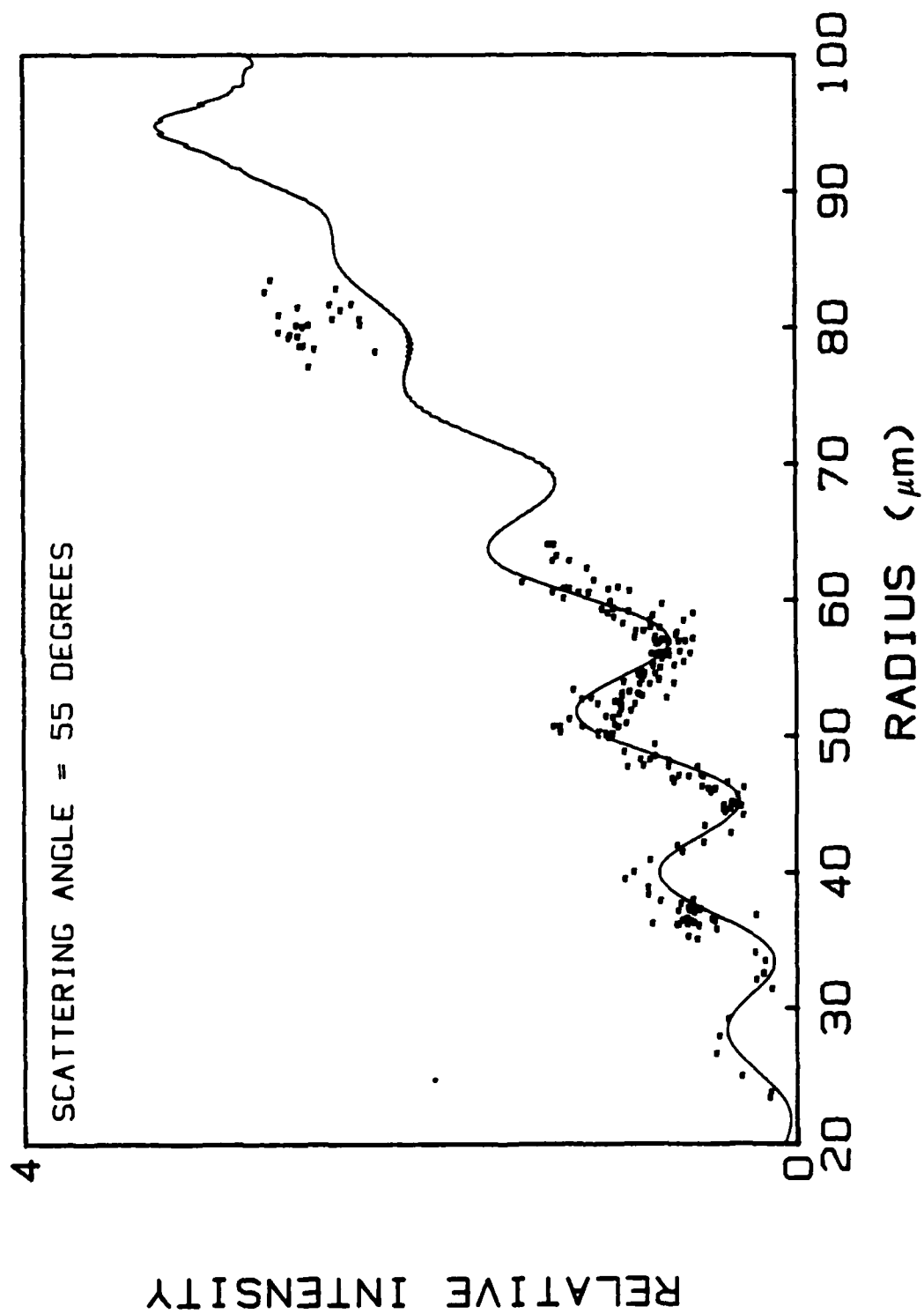


FIG. 15. Intensity and radius with data shifted to match theory at  $56.9\mu\text{m}$ .

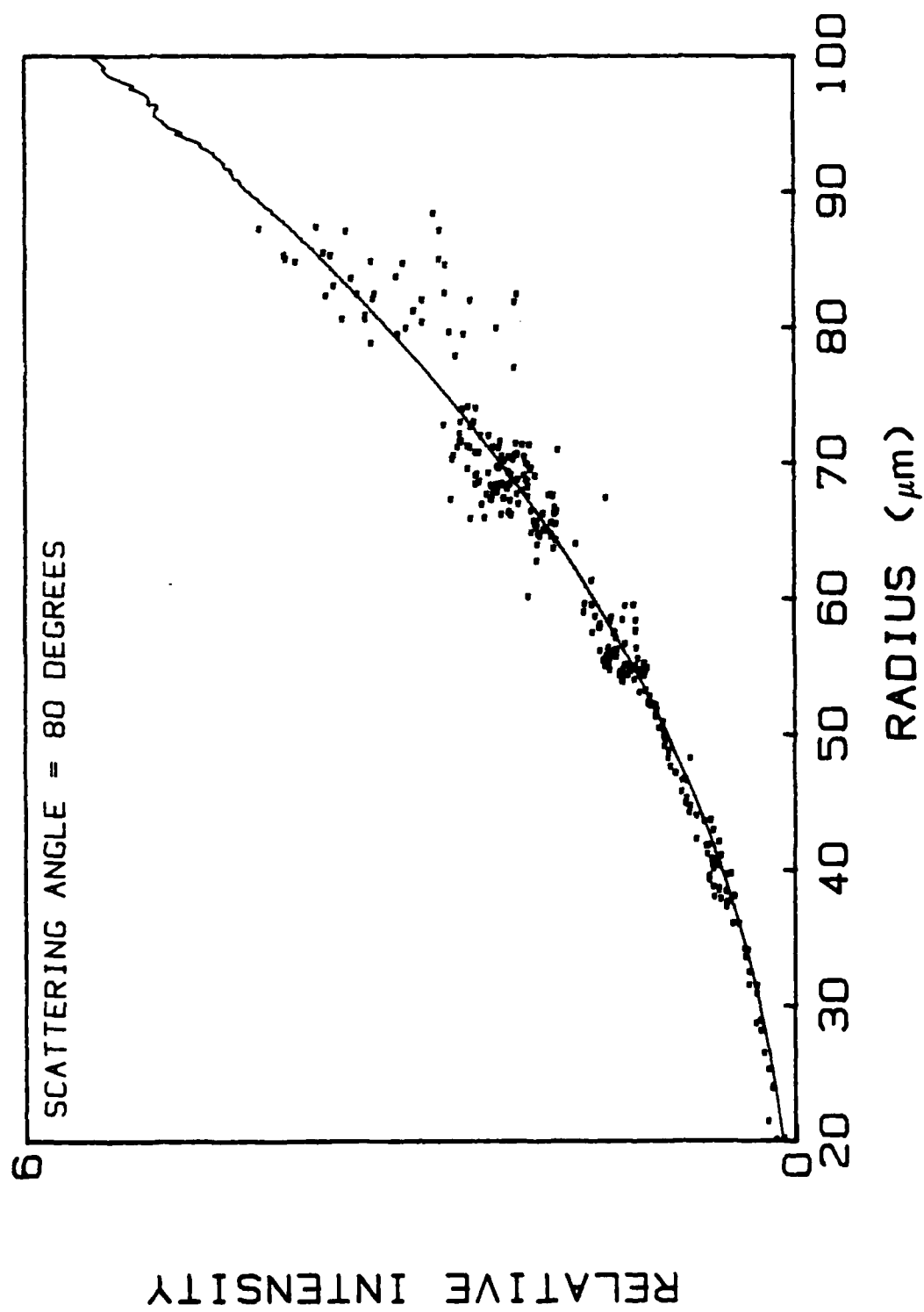


FIG. 16. Intensity and radius at scattering angle = 80 degrees, same shift as in Fig. 15.



### III. DISCUSSION

The results of this study showed that accurate radial measurements of single air bubbles could be achieved with a Mie scattering technique. Using the relative light intensity scattered at 80 degrees the relationship

$$\text{Radius} = 50.1(\text{Relative Intensity})^{.404}$$

could be used to obtain the radius. This method gave the radius of the bubble to within an estimated 3% for bubbles of radii less than 80  $\mu\text{m}$ .

The estimated 3% was a summation of the possible sources of error in the light scattering measurements. The major source (as much as 2.0%) was the  $\pm 0.25$  degree angle measurement error. The next largest source was in the voltage readings. For 100 readings the standard deviation divided by the mean was approximately 1.0%, which translates into a less than 1% radius error for the entire range of bubble sizes. These fluctuations were probably due to the oscillation of the bubble, background scatterers, changing bubble size, and noise in the electronics. The numerical integration and the acceptance angle measurement added the next most significant portion.

The other small sources of error fell into two categories. Those due to assumptions made prior to the calculations and those due to the experimental arrangement. Three assumptions were made prior to the computations. First, the index of refraction of the water relative to

the air was assumed to not vary significantly from 1.33. Second, absorption of the light by the air in the bubble was ignored. Third, the bubble interface was assumed to be pure air-water, i.e. no surface contaminants.

Some small errors were inherent in the experimental setup. A small component of the perpendicular field may have been detected. This component could arise from inaccurate horizontal alignment of the E-field. Inaccurate leveling of the laser beam could change the scattering plane which would introduce a  $\phi$  component. This problem could also arise from a deviation in the glass cylinder. A source of error that was probably most prevalent in the large bubbles ( $> 80 \mu\text{m}$ ) is the fact that bubbles oscillating with a great enough amplitude have an average radius that is larger than the stationary radius.<sup>1</sup> The radius measured was assumed to be the average radius, which was equal to the stationary radius. This effect may have been a minor cause of the data scatter in the large bubble region.

Another source of error was any nonlinearity in the photodiode's response curve. A rough check of the photodiode linearity was conducted. The results did not indicate that the response was nonlinear over the range of input intensities used in the actual measurements. There was, however, a nonlinearity in the response over the range used for the measurements of the beam profile and the single slit diffraction pattern. This nonlinearity could account for some of the deviation of the experimental points from the theory in the single slit diffraction pattern shown in Fig. 13. The deviation from theory of this pattern

could also come from the glass cover slips used in the slit holder or from an error in the slit width measurement.

The results presented here suggested that work done by Crum,<sup>8</sup> in which the rise-velocity method was used, with a rigid sphere drag law, is indeed incorrect by as much as 10%. The causes of the 10% deviation of the rise-velocity radius from the light intensity radius in this experiment could be due to several factors. The major source of error was considered to be the choice of a rigid sphere drag law. The results of this experiment indicated that there was a larger drag coefficient for air bubbles, of less than 100  $\mu\text{m}$ , than is predicted by a rigid sphere drag law. The departure from rigid sphere drag laws is known to exist for large bubbles,<sup>10</sup> but data are absent for the bubble sizes used in this experiment. Another source of the deviation is the short time difference between light intensity and rise-velocity measurements. Also any change in the temperature of the water during a data run was ignored.

Although this Mie scattering method is theoretically feasible for all bubble sizes there was an exceedingly large amount of data scatter for large bubbles. This lack of correlation was assumed to be a result of experimental errors in the rise-velocity measurement since the Mie scattering theory has been shown to be accurate.<sup>13</sup> The experimental error was greatest for large bubbles due to the fact that the reaction time errors were larger for large bubbles and the fact that large bubbles were harder to keep stationary in the laser beam.

Despite the lack of correlation for large bubbles the Mie scattering method was superior to the rise-velocity method for measuring the radii of air bubbles, even if the correct drag law had been known. The Mie scattering method was precise (estimated 1% error) and once calibrated required the measurement of only a single parameter. It also did not disturb the bubble, if light pressure was ignored. It was also fast; data points (100 readings/point) could be taken in about 0.5 second. This speed reduces the change in the radius during a measurement.

The principal disadvantage of this technique lies in the need for specialized equipment and precision optical alignment. The only other drawback with the method was the need to use the rise-velocity method for an initial calibration. Before the intensity relative to the intensity at 50  $\mu\text{m}$  could be calculated the intensity of 50  $\mu\text{m}$  was required. This was accomplished by making rise-velocity radius measurements in conjunction with light intensity measurements at 55 degrees. This 55 degree data supplied the correlation that allowed the 80 degree intensity to be used for direct measurements of radius.

Initially, the idea was to use the ratio of the light intensity readings from two photodiodes, one at 55 degrees the other at 80 degrees. This ratio from a single bubble, followed through a range of sizes, would have located the point on the ratio curve accurately. This method would also have entirely eliminated the need to obtain the rise-velocity. Unfortunately a set of matched photodiodes were not available (lack of foresight on my part). With photodiodes of different responsivities it was not possible to obtain ratios of one (for the same

input) over the range of inputs.

Besides the use for measuring radius directly this method has other applications. With an independent measure of the radius and an accurate measure of the rise-velocity, the drag coefficient can be experimentally determined. An accurate measure of the radius of a bubble can also be used to make a measurement of the damping on an oscillating sphere, which has not been accurately measured. There are two ways this damping can be measured. First, the radius at which the harmonic resonance occurs can be found. This radius when matched to the predicted radius, which contains the damping and some other measurable parameters, will give the damping. The method may also be refined to allow the direct measurement of the oscillation amplitude, which is a function of the damping. The damping is of interest particularly for high vapor-pressure liquids.<sup>5</sup>

Finally, there are a few modifications which should be done to the present setup to improve the ease, accuracy, and repeatability of the method. A precalibrated angle measurement device would reduce the error by about 2%. A pair of matched photodiodes and preamps are needed to allow for ratio measurements. A wider laser beam would eliminate the error caused by improperly centering the bubble in the beam. With a wider beam there also exists the possibility of using a suspended glass bead for calibration purposes. Since the scattering pattern is sensitive to the relative index of refraction, any measurements which are to be made on other than pure substances will require a means of measuring the

index of refraction of the mixture. For example, mixtures of high vapor pressure substances (like alcohols) with water could be used to measure vapor effects on damping.

## REFERENCES

1. A. Prosperetti. "Nonlinear oscillations of gas bubbles in liquids: steady-state solutions." J. Acoust. Soc. Am. 56, 878-885 (1974).
2. A. Prosperetti. "Application of the subharmonic threshold to the measurement of the damping of oscillating gas bubbles." J. Acoust. Soc. Am. 61, 11-16 (1977).
3. A. Prosperetti. "Thermal effects and Damping mechanisms in the forced radial oscillations of gas bubbles in liquids." J. Acoust. Soc. Am. 61, 17-27 (1977).
4. L.A. Crum. "Measurements of the growth of air bubbles by rectified diffusion." J. Acoust. Soc. Am. 68, 203-211 (1980).
5. M. Fanelli, A. Prosperetti, and M. Realì. "Radial oscillations of gas-vapor bubbles in liquids. Part I: Mathematical Formulation." Acustica 47, 253-265 (1981).
6. L.A. Crum and G.M. Hansen. "Generalized equations for rectified diffusion." J. Acoust. Soc. Am. 72, 1586-1592 (1982).
7. L.A. Crum. "The polytropic exponent of gas contained within air bubbles pulsating in a liquid." J. Acoust. Soc. Am. 73, 116-120 (1983).
8. L.A. Crum and A. Prosperetti. "Nonlinear oscillation of gas bubbles in liquids: An interpretation of some experimental results." J. Acoust. Soc. Am. 73, 121-127 (1983).
9. L.A. Crum and G.M. Hansen. "Growth of air bubbles in tissue by rectified diffusion." Phys. Med. Biol. 27, 413-417 (1982).
10. R. Clift, J.R. Grace, and M.E. Weber. Bubbles, Drops and Particles (Academic, New York, 1978).
11. R.K. Gould. "Rectified diffusion in the presence of, and absence of, acoustic streaming." J. Acoust. Soc. Am. 56, 1740-1746 (1974).
12. P.L. Marston. "Critical angle scattering by a bubble: Physical-optics approximation and observations." J. Opt. Soc. Am. 69, 1205-1211 (1979).

13. D.S. Langley and P.L. Marston. "Critical-angle scattering of laser light from bubbles in water: measurements, models, and application to sizing of bubbles." *Appl. Opt.* 23, 1044-1054 (1984).
14. P. Debye. "Der lichtdruck auf kugeln von beliebigem material." *Ann. Phys.* 30, 57-136 (1909).
15. G. Mie. "Beitrage fur optik truber medier, speziell kolloidaler metallosungen." *Ann. Phys.* 25, 377-445 (1908).
16. D. Deirmendjian. "Scattering and polarization properties of water clouds and hazes in the visible and infrared." *Appl. Opt.* 3, 187-196 (1964).
17. R. Eider. "The elliptical polarization of light scattered by a volume of atmospheric air." *Appl. Opt.* 5, 569-575 (1966).
18. T.S. Fahler and H.C. Bryant. "Optical back scattering from single water droplets." *J. Opt. Soc. Am.* 58, 304-310 (1968).
19. R. Penndorf. "Mie scattering coefficient for water droplets in air." *J. Meteorology* 13, 219-220 (1956).
20. E. Bauer. "The scattering of infrared radiation from clouds." *Appl. Opt.* 3, 197-202 (1964).
21. J.C. Johnson and J.R. Terrell. "Transmission cross sections for water spheres illuminated by infrared radiation." *J. Opt. Soc. Am.* 45, 451-454 (1955).
22. F.C. Chromey. "Evaluation of Mie equations for colored spheres." *J. Opt. Soc. Am.* 50, 730-737 (1960).
23. V.R. Stull and G.N. Plass. "Emissivity of dispersed carbon particles." *J. Opt. Soc. Am.* 50, 121-129 (1960).
24. D.L. Kingsbury and P.L. Marston. "Mie scattering near the critical angle of bubbles in water." *J. Opt. Soc. Am.* 71, 358-361 (1981).
25. D. Holve and S.A. Self. "Optical particle sizing for in situ measurements." *Appl. Opt.* 18, 1632-1645 (1972).
26. H.C. Van de Hulst. Light Scattering by Small Particles. (Wiley, New York, 1957).
27. M. Kerker. The scattering of light and other electromagnetic radiation. (Academic, New York, 1969).



28. L.M. Milne-Thomson. Theoretical Hydrodynamics. (Macmillan, New York, 1968).
29. L.A. Crum and A.I. Eller "Motion of bubbles in stationary sound fields." J. Acoust. Soc. Am. 48, 181-189 (1970).
30. M. Born and E. Wolf. Principles of Optics (Pergamon, New York, 1959).
31. J. Stratton. Electromagnetic Theory. (McGraw Hill, New York, 1941).
32. M. Abramowitz and I.A. Stegun. Handbook of Mathematical Functions (Cambridge, London, 1922).
33. G.N. Watson. A Treatise on the Theory of Bessel Functions. (Cambridge, London, 1922).
34. J.V. Dave. "Scattering of electromagnetic radiation by a large, absorbing sphere." IBM J. Res. Develop. May (1969).
35. G.E. Davis. "Scattering of light by an air bubble in water." J. Opt. Soc. Am. 45, 572-581 (1955).
36. G.W. Kattawar and G.N. Plass. "Electromagnetic scattering from absorbing spheres." Appl. Opt. 6, 1377-1389 (1967).
37. W.J. Wiscombe. "Improved Mie scattering algorithms." Appl. Opt. 19, 1505-1509 (1980).
38. G.N. Plass. "Mie scattering and absorption cross sections for absorbing particles." Appl. Opt. 5, 279-285 (1966).
39. J.R. Hodgkinson and I. Greenleaves. "Computations of light-scattering and extinction by spheres according to diffraction and geometrical optics, and some comparisons with Mie theory." J. Opt. Soc. Am. 53, 577-588 (1963).
40. F.J. Corbato and J.L. Uretsky. "Generation of spherical Bessel functions in digital computers." J. Assoc. Computing Machinery 6, 366-375 (1959).
41. J.C.P. Miller. British Association for the Advancement of Science, Mathematical Tables, Vol. X, Bessel Functions, Part II. (Cambridge, London, 1952).

## APPENDIX A

Following is a listing of the program used to make the Mie scattering calculations. The program when run requires the input of several parameters, M, IRS, IRF, IRI, IDS, IDF, IDI, IOUT.

M, is the relative index of refraction

IRS, is the starting radius times 10 (ex. 10 microns is input as 100)

IRF, is the final radius times 10

IRI, is the radius increments times 10

IDS, is the starting angle in degrees times 100 (ex. 20 degrees is input as 2000)

IDF, is the final angle times 100

IDI, is the degree increments times 100

IOUT, is the output format desired, IOUT=1 gives deg,G2, IOUT=2 gives radius,G2

This program was altered slightly to give the numerical integrations.

FILE: MIE      FORTRAN A1 CMS-OLE MISS

```

      IMPLICIT REAL*8(A-H,C-Z)
      IMPLICIT INTEGER(I-N)
      REAL*8 RJA(3000),RJE(3000),P(3000),J(3000)
      REAL*8 JO,INTENS,M
      COMPLEX*16 Z8,Z9,HA0,HA1,HA2,LITA,LITB,NWF,TCP,S2,S1,HPA
      COMPLEX*16 LITA1,LITA2,LITB1,LITB2,SC
      INTEGER LAM,NEW
      Z8=(1.D0,0.D0)
      Z9=(0.D0,1.D0)
      FI=3.14159D0
      READ*,M,IRS,IRF,IRI,IDS,IDF,IDI,IOUT
      DO 88 IR=IRS,IRF,IRI
      RAD=IR*.1D0*1.D-06
      FOUT=IR*.1D0
      A=2.D0*PI*1.33*RAD/6.326D-07
      B=A*M
      BIGN=A+2.+(4.05*(A**.333))
      N9=IDINT(BIGN)
      S8=DSIN(A)/A
      S9=DCOS(A)/A
      II=1
      X=A
      GOTO 400
10    DO 41 I=1,LAM
41    RJA(I)=PA*J(I)
      I=LAM
42    RJA(I+1)=R(I)*RJA(I)
      IF (RJA(I+1).LT.1.E-77) GOTO 60
      I=I+1
      GOTO 42
60    II=2
      X=P
      GOTO 400
20    DO 43 I=1,LAM
      RJE(I)=PA*J(I)
43    CONTINUE
      I=LAM
44    RJB(I+1)=R(I)*RJB(I)
      IF (RJB(I+1).LT.1.E-77) GOTO 70
      I=I+1
      GOTO 44
70    CONTINUE
      DO 88 IDEG=IDS,IDF,IDI
      S2=(0.D0,0.D0)

```

```

S0=S2
S1=S2
QSCA=0.0D0
P0=0.0D0
P1=0.0D0
PP0=0.0D0
PP1=0.0D0
YA0=S8
YA1=-S9
DEG=IDEG/100.00
TH=DEG/57.29578D0
C=DCOS(TH)
N=1
48  CONTINUE
    SA=A*RJA(N)
    SB=E*EJB(N)
    IF(YA1.LT.-1.0E70) GOTO501
    YA2=(2.0D0*N-1.0D0)*YA1/A-YA0
502  CONTINUE
    HA2=RJA(N)-Z9*YA2
    IF(N.EQ.1) GOTO 500
    HA1=RJA(N-1)-Z9*YA1
    P2=C*P1*(2.0D0*N-1.0D0)/(N-1.0D0)-P0*N/(N-1.0D0)
    PP2=(2.0D0*N-1.0D0)*P1+PP0
    AJP=RJA(N-1)-(N+1.0D0)*RJA(N)/A
    BJB=EJB(N-1)-(N+1.0D0)*EJB(N)/B
30   CONTINUE
    EIE=-P2
    TAO=-C*P2-(C*C-1.0D0)*PP2
    HPA=HA1-(N+1.0D0)*HA2/A
    SPA=A*AJP+RJA(N)
    SPB=B*BJB+RJB(N)
    TCP=A*HPA+HA2
    LITA1=(SA*SPB)-(M*SB*SPA)
    LITA2=A*HA2*SPB-M*SE*TCP
    YTESTA=REAL(LITA2)
    YTESTA=DABS(YTESTA)
    IF(YTESTA.LT.1.0E-70) GOTO503
504  CONTINUE
    LITA=LITA1/LITA2
    LITB1=M*SA*SPB-SB*SPA
    LITB2=M*A*HA2*SPB-SE*TCP
    YTESTB=REAL(LITB2)
    YTESTB=DABS(YTESTB)
    IF(YTESTB.LT.1.E-70) GOTO505
506  CONTINUE
    LITE=LITE1/LITB2

```

```

NWP=LITA*TAO+LITB*PIE
S2=NWP*(2.D0*N+1.D0)/N/(N+1.D0)+S2
S1=(2.D0*N+1.D0)/N/(N+1.D0)*(LITA*PIE+LITB*TAO)+S1
S0=S0+(2.D0*N+1.D0)*(LITA+LITB)
TEST=LITA*DCONJG(LITA)+LITB*DCONJG(LITB)
IF (TEST.LT.1.E-20) GOTO 50
QSCA=QSCA+(2.D0*N+1.D0)*TEST
P0=P1
P1=P2
PP0=PP1
PP1=PP2
YAO=YAI
YAI=YAI
N=N+1
IF (N.GT.N9) GOTO 50
GOTO 48
50 CONTINUE
RHO=2.*A*(M-1.)
QSCA=QSCA*2./A/A
INTENS=S2*DCONJG(S2)
GCNE=S1*DCONJG(S1)
GONE=GONE*4./A/A
GCNE=DLOG10(GONE)
GTWO=DLOG10(4.*INTENS/A/A)
SOUT=S0*DCONJG(S0)
SOUT=DLOG10(SOUT*.25)
IF (IOUT.EQ.2) GOTO 600
WRITE(6,101) DEG
WRITE(6,101) GTWO
WRITE(11,100) DEG,GONE
WRITE(12,100) DEG,GTWO
GOTO 88
600 WRITE(6,100) ROUT,GONE
WRITE(11,100) ROUT,GCNE
WRITE(12,100) ROUT,GTWC
88 CONTINUE
STCP
100 FORMAT(2X,F6.2,F10.5)
101 FORMAT(2X,F10.5)
102 FORMAT(2X,3E13.6)
138 FORMAT(2X,I4,2E17.6)
139 FORMAT(2X,I4,E17.10)
500 AJF=S8-2.D0*RJA(1)/A
BJP=DSIN(B)/B-2.D0*RJB(1)/B
HAI=S8-29*YAI
P2=1.D0
PP2=0.D0

```

```

      GOTO 30
501  YA 2=YA 1
      GOTO 502
400  UPR=2.D0*X/(2.D0*BIGN+1.D0)
      ENEW=DLOG(1.E-9*(.1+.35*UPR*(2.-UPR*UPR)/2./(2.-UPR*UPR)))
      ENEW=BIGN-ENEW/.693
      NEW=IDINT(ENEW)
401  NEW=NEW+25
402  R(NEW)=0.
      I=NEW
410  R(I-1)=X/(2.D0*I+1.D0-X*R(I))
      IF(R(I-1).GT.1.) GOTO 420
      IF(I.EQ.2) GOTO 401
      I=I-1
      GOTO 410
420  LAM=I-1
      J(LAM+1)=R(LAM)
      J(LAM)=1.D0
      I=LAM
430  J(I-1)=(2.D0*I+1.D0)/X*J(I)-J(I+1)
      I=I-1
      IF(I.EQ.1) GOTO 440
      GOTO 430
440  J0=(3.D0/X)*J(1)-J(2)
      PA=DSIN(X)/X/J0
      IF(II.EQ.1) GOTO 10
      GOTO 20
503  LITA 2=Z8*1.D-70+Z9*1.E-66
      GOTO 504
505  LITB 2=Z8*1.D-70+Z9*1.D-66
      GOTO 506
      END

```

BIOGRAPHICAL SKETCH OF THE AUTHOR

Gary Michael Hansen

Candidate for the degree of  
Doctor of Philosophy

PERSONAL: Born February 13, 1956 in Berwyn, Illinois.  
the son of Ervin and Margaret Hansen.

EDUCATION: Bachelor of Arts in Physics, Lewis University; Romeoville  
Illinois. May 1978.  
Master of Science in Physics, Southern Illinois  
University; Carbondale, Illinois. May 1980

HONORS: Member of the Sigma Pi Sigma and the Phi Kappa Phi honor  
societies.

CAREER  
OBJECTIVES: To become a contributing member of a research group that  
is doing work in physical acoustics or a related field.

ADDRESS: 1419 Van Buren Avenue  
Oxford, Mississippi 38655

February 1983

REPORTS DISTRIBUTION LIST FOR ONR PHYSICS DIVISION OFFICE  
UNCLASSIFIED CONTRACTS

Director Defense Advanced Research Projects Agency Attn: Technical Library 1400 Wilson Blvd. Arlington, Virginia 22209	3 copies
Office of Naval Research Physics Division Office (Code 412) 800 North Quincy Street Arlington, Virginia 22217	3 copies
Office of Naval Research Director, Technology (Code 200) 800 North Quincy Street Arlington, Virginia 22217	1 copy
Naval Research Laboratory Department of the Navy Attn: Technical Library Washington, DC 20375	3 copies
Office of the Director of Defense Research and Engineering Information Office Library Branch The Pentagon Washington, DC 20301	3 copies
U. S. Army Research Office Box 1211 Research Triangle Park North Carolina 27709	2 copies
Defense Technical Information Center Cameron Station Alexandria, Virginia 22314	12 copies
Director, National Bureau of Standards Attn: Technical Library Washington, DC 20234	1 copy
Commanding Officer Office of Naval Research Western Detachment Office 1030 East Green Street Pasadena, California 91101	3 copies
Commanding Officer Office of Naval Research Eastern/Central Detachment Office 495 Summer Street Boston, Massachusetts 02210	3 copies



Commandant of the Marine Corps Scientific Advisor (Code RD-1) Washington, DC 20380	1 copy
Naval Ordnance Station Technical Library Indian Head, Maryland 20640	1 copy
Naval Postgraduate School Technical Library (Code 0212) Monterey, California 93940	1 copy
Naval Missile Center Technical Library (Code 5632.2) Point Mugu, California 93010	1 copy
Naval Ordnance Station Technical Library Louisville, Kentucky 40214	1 copy
Commanding Officer Naval Ocean Research & Development Activity Technical Library NSTL Station, Mississippi 39529	1 copy
Naval Explosive Ordnance Disposal Facility Technical Library Indian Head, Maryland 20640	1 copy
Naval Ocean Systems Center Technical Library San Diego, California 92152	1 copy
Naval Surface Weapons Center Technical Library Silver Spring, Maryland 20910	1 copy
Naval Ship Research and Development Center Central Library (Code L42 and L43) Bethesda, Maryland 20084	1 copy
Naval Avionics Facility Technical Library Indianapolis, Indiana 46218	1 copy

FILED

8